

1-29-2009

# Analysis, design, and implementation of a reconfigurable fractal volumetric left-handed metamaterial

Teofilo Max De La Mata Luque

Follow this and additional works at: [https://digitalrepository.unm.edu/ece\\_etds](https://digitalrepository.unm.edu/ece_etds)

---

## Recommended Citation

De La Mata Luque, Teofilo Max. "Analysis, design, and implementation of a reconfigurable fractal volumetric left-handed metamaterial." (2009). [https://digitalrepository.unm.edu/ece\\_etds/66](https://digitalrepository.unm.edu/ece_etds/66)

This Thesis is brought to you for free and open access by the Engineering ETDs at UNM Digital Repository. It has been accepted for inclusion in Electrical and Computer Engineering ETDs by an authorized administrator of UNM Digital Repository. For more information, please contact [disc@unm.edu](mailto:disc@unm.edu).

**Teofilo Max De la Mata Luque**

*Candidate*

---

**Electrical & Computer Engineering**

*Department*

---

This thesis is approved, and it is acceptable in quality and form for publication on microfilm:

*Approved by the Thesis Committee:*

Prof. Christos G. Chistodoulou, Chairperson

---

Prof. Mark A. Gilmore

---

Prof. Ihab F. El Kady

---

---

---

---

---

---

---

Accepted:

\_\_\_\_\_  
*Dean, Graduate School*

\_\_\_\_\_  
*Date*

**ANALYSIS, DESIGN AND IMPLEMENTATION OF A  
RECONFIGURABLE FRACTAL VOLUMETRIC  
LEFT-HANDED METAMATERIAL**

**BY**

**TEOFILO MAX DE LA MATA LUQUE**

**B.E., ELECTRICAL & ELECTRONICS ENGINEERING,  
PONTIFICIA UNIVERSIDAD CATÓLICA DEL PERÚ, 2003**

**PROFESSIONAL DEGREE IN ELECTRICAL &  
ELECTRONICS ENGINEERING, PONTIFICIA  
UNIVERSIDAD CATÓLICA DEL PERÚ, 2006**

THESIS

Submitted in Partial Fulfillment of the  
Requirements for the Degree of

**Master of Science**

**Electrical Engineering**

The University of New Mexico  
Albuquerque, New Mexico

**December, 2008**

**©2008, Teofilo Max De la Mata Luque**

To God for giving me life and health

To my parents Norma and Pepe for their unconditional love and support along my life

To my advisor Christos G. Christodoulou for giving me the tools and facilities to accomplish this work, supervising it, and also for financially supporting me, I am greatly indebted to him

To my colleague Naga R. Devarapalli for several fruitful discussions, suggestions, ideas, and even hands-on work; I am very thankful for his selfless help

To my colleagues Sergio, Joseph, Prashanth, Yue and Ralph for directly collaborating on this thesis through their teachings, ideas, suggestions and hardware loans

To my friends and relatives Dione, Lutgarda, Nery, Karla, Amalia, Hilda, Jorge, Daniel, Akio, Jaime, Alonzo, Victor, Christopher, Javier, Efren and Pedro for their emotional support, for their help in one way or another and for all those little big moments every single day

To all of them, my deepest gratitude

**ANALYSIS, DESIGN AND IMPLEMENTATION OF A  
RECONFIGURABLE FRACTAL VOLUMETRIC  
LEFT-HANDED METAMATERIAL**

**BY**

**TEOFILO MAX DE LA MATA LUQUE**

**ABSTRACT OF THESIS**

Submitted in Partial Fulfillment of the  
Requirements for the Degree of

**Master of Science  
Electrical Engineering**

The University of New Mexico  
Albuquerque, New Mexico

**December, 2008**

# **Analysis, design and implementation of a Reconfigurable Fractal Volumetric Left-handed Metamaterial**

by

**Teofilo Max De la Mata Luque**

B.E., Electrical & Electronics Engineering,  
Pontificia Universidad Católica del Perú, 2003

Professional Degree in Electrical & Electronics Engineering,  
Pontificia Universidad Católica del Perú, 2006

M.Sc., Electrical Engineering, The University of New Mexico, 2008

## **ABSTRACT**

At the present time, one of the greatest goals to exploit the advantages of Volumetric Left-handed Metamaterials (LHM) is overcoming their very narrow operational bandwidth. This thesis proposes two schemes to efficiently solve this difficulty: 1) a mechanism which reconfigures, at will, the frequency the LHM operates at, and 2) a novel arrangement of Split Ring Resonators (SRR) based on the Sierpiński carpet fractal pattern with two SRR sizes. Reconfigurability is implemented by cutting two splits of

different widths in each ring of the SRRs. These SRRs are simulated with switches in the ON and OFF states inside an ideal simulation environment implemented in the electromagnetic modeling software HFSS where the reflection and transmission coefficients are calculated. Through simulations, each size of SRR is independently optimized and shown to have a broad frequency range where its resonance can be selected from. The two SRRs are subsequently combined in a single structure according to the Sierpiński carpet fractal pattern. This structure is simulated again to obtain a new frequency response with two resonance frequencies near each other. A thin-wire structure is designed and coalesced with the fractal structure which results in a LHM with two transmission bands. Finally, prototypes are fabricated by mechanically etching high-frequency laminates, and tested using standard techniques. Experimental results demonstrate that the fabricated LHM is characterized by two well-defined left-handed transmission bands. Both experimental and theoretical results show a good agreement in predicting the resonances of the complex LHM structure.

# TABLE OF CONTENTS

<b>INTRODUCTION.....</b>	<b>1</b>
<b>CHAPTER 1</b>	
<b>THEORETICAL FRAMEWORK AND CHARACTERIZATION .....</b>	<b>6</b>
1.1 Volumetric Left-Handed Metamaterials .....	10
1.2 Bandwidth enhancement .....	17
1.2.1 Sierpiński carpet fractal pattern .....	18
1.2.2 Reconfigurability .....	20
<b>CHAPTER 2</b>	
<b>DESIGN &amp; SIMULATION.....</b>	<b>22</b>
2.1 Plane wave port generation and Master/Slave boundary conditions .....	23
2.2 Reconfigurable SRR design and simulation .....	27
2.2.1 Large SRR.....	30
2.2.2 Small SRR.....	36
2.3 Sierpiński-carpet-arranged SRRs design and simulation.....	40
2.4 Thin-wire structure design and simulation .....	44
2.5 Left-handed metamaterial simulation .....	49

## **CHAPTER 3**

<b>EXPERIMENTAL RESULTS.....</b>	<b>52</b>
3.1 PCB Fabrication.....	53
3.2 S-parameters measurement setup.....	58
3.3 Measurements .....	63
3.4 Comparison and conclusions .....	65
<b>CONCLUSIONS AND FUTURE WORK.....</b>	<b>71</b>
<b>APPENDIX.....</b>	<b>73</b>
Appendix A: HFSS Simulation files.....	73
Appendix B: Autocad & PCB files.....	74
<b>REFERENCES.....</b>	<b>75</b>

# INTRODUCTION

What is a “Metamaterial”? Recently, there has been a growing interest in fabricated structures and composite materials that either imitate known material responses or qualitatively have new, physically realizable response functions that do not occur or may not be easily available in nature. The unconventional response functions of these Metamaterials (MTM) are often generated by artificially fabricated inclusions embedded in a host medium or connected to host surface. Exotic properties for such materials have been predicted; many experiments have confirmed the basic knowledge of many of them. The underlying interest in MTM is the potential to have the ability to engineer the electromagnetic and optical properties of materials for a variety of applications. The impact of MTM may be enormous: If one can tailor and manipulate the wave properties, significant decreases in size and weight components, devices and systems along with enhancements in their performance appear to be realizable.

In a certain way, every material is a composite, even if the individual ingredients consist of atoms and molecules. The original purpose in defining a permittivity and permeability was to get a homogeneous view of electromagnetic properties of the medium. Therefore, it is only a small step to replace the atoms of the original concept with structure on a larger scale. If periodic structures are considered, the contents of a period of the structure (which will be called unit cell) will define the effective response of the system as a whole, but, clearly, some constraints on the period’s size must exist.

The first attempt to explore the concept of “artificial” materials appears to trace back to the late part of the nineteenth century when in 1898 Jagadis Chunder Bose conducted the first microwave experiment on twisted structures (nowadays known as chiral geometries). In 1914, Karl Ferdinand Lindman worked on “artificial” chiral media by embedding many randomly oriented small wire helices in a host medium [1]. In 1948, Kock [2] made lightweight microwave lenses by arranging conducting spheres, disks, and strips periodically and effectively tailoring the effective refractive index of the artificial media. Artificial chiral Metamaterials were extensively investigated in the 1980s and 1990s for microwave radar absorbers and other applications. Since then, artificial complex materials have been the subject of research for many investigators worldwide. In recent years new concepts in synthesis and novel fabrication techniques have allowed the construction of structures and composite and these MTM can in principle be synthesized by embedding various constituents/inclusions with novel geometric shapes and forms in some host media. Various types of electromagnetic composite media, such as left-handed materials, chiral materials, omega media, wire media, bianisotropic media, linear and nonlinear media, and local and nonlocal media, to name a few, have been studied by various research groups worldwide.

Recently, the idea of complex materials in which both the permittivity and the permeability possess negative real values at certain frequencies has received considerable attention. In 1967, Veselago theoretically investigated plane-wave propagation in a material whose permittivity and permeability were assumed to be simultaneously

negative [3]. For MTMs with negative permittivity and permeability, several names and terminologies have been suggested, such as “left-handed” media, media with negative refractive index (NIR), “backward-wave media” (BW media) and “double-negative (DNG)” metamaterials, to name a few. In this work, from now on, MTMs with negative permittivity and permeability, and hence negative index of refraction, will be referred indistinctly as left-handed Metamaterials (LHM) or Metamaterials (MTM).

Many research groups all over the world are now studying various aspects of LHM, and several ideas and suggestions for future applications of these materials have been proposed. The index of refraction of a LHM has been shown theoretically to be negative by several groups (e.g. [4]), and several experimental studies have been reported confirming this negative-index-of-refraction (NIR) property and applications derived from it, such as phase compensation and electrically small resonators [5], negative angles of refraction [6], sub-wavelength waveguides with lateral dimension below diffraction limits [7], enhanced focusing [8], backward-wave antennas [9], Cerenkov radiation [10], photon tunneling [11], and enhanced electrically small antennas [12]. These studies rely heavily on the concept that a continuous-wave (CW) excitation of a LHM leads to a NIR and, hence, to negative or compensated phase terms.

When a LHM is built in a three dimensional fashion, filling a volume and taking the shape of a cube or brick, it is generally called Volumetric Left-handed Metamaterial. A Volumetric LHM can be manufactured with a grid of very thin wires that can behave like a plasma medium to provide an effective negative electric permittivity [13] interspaced

with a periodic array of split ring resonators (SRRs) to provide an effective negative magnetic permeability [14].

To date, LHMs have a very limited bandwidth because it is the consequence of the very sharp resonance of SRRs. The aim of this thesis is to improve the bandwidth of these Metamaterials by placing SRRs of two different sizes and arranging them following a fractal pattern. As a result if two resonances are obtained, located close enough to each other, a wider band of NIR can be achieved. Moreover, one can allow the resonance frequencies to be adjusted or tuned by opening and closing switches inside the SRR structures. This approach opens and closes the splits of the rings and allows one to change the value of resonance to match the requirements of a particular design.

The thesis is divided in three main chapters. In Chapter 1, some of the basic theory and important concepts are discussed. Also, a comprehensive description and characteristics of one dimensional volumetric LHM, which is the material in development, along with some formulas for Euclidean geometry inclusions will be presented. Finally in Chapter 1, enhancements are proposed and qualitatively explained in full detail. In Chapter 2, the design and simulations process are carried out. Firstly, using the electromagnetic modeling and design software HFSS, the simulations conditions are created using the appropriate boundary conditions and ports. Then, the reconfigurable SRRs are design following certain theoretical models studied in Chapter 1 and, through simulations; the final model is optimized. Then, using the Sierpiński-carpet fractal pattern, SRRs are arranged and simulated again in order to achieve the two-adjacent-resonance goal.

Finally, thin-wire structures are also simulated using the same procedure as the one of the SRRs and, at the end, both are combined into a single structure to form the MTM. In Chapter 3, all the experimental results are presented and discussed. The thesis ends with the conclusions.

# CHAPTER 1

## THEORETICAL FRAMEWORK AND CHARACTERIZATION

In composite media, EM waves interact with the inclusions, inducing electric and magnetic moments, which in turn change the macroscopic effective permittivity and permeability of the bulk composite medium. Since MTMs can be synthesized by embedding artificially fabricated inclusions in a specified host medium or on a host surface, this provides the designer with a large collection of independent parameters (or degrees of freedom) to work with in order to engineer a MTM with specific electromagnetic response functions not found in each of the individual constituents. Parameters such as the properties of the host material; the size, shape, and composition of the inclusions; and the density, arrangement, and alignment of these inclusions can be modified giving rise to a new MTM; among these, the geometry of the inclusions is one that can provide a variety of new possibilities for MTMs processing.

Left-handed Metamaterials (LHM) were first theoretically idealized by Veselago in 1967 [3]. He showed that for a monochromatic uniform plane wave in such a medium the direction of the Poynting vector is anti-parallel to the direction of the phase velocity, contrary to the case of plane wave propagation in conventional simple media; but a physical realization was reported many years later, in 2000 by Smith [15], while an

experimental verification of negative refraction occurred during the following year, 2001, by Shelby [6].

Since LHM have been recently developed, very little theory and mathematical models have been created so far. Up to now, no actual books on the topic have been written either, but many researches and experiments have been conducted and a very comprehensive summary of them can be found on [16]. According to it, the response of a system to the presence of an electromagnetic field is determined to a large extent by its macroscopic parameters permittivity  $\epsilon$  and permeability  $\mu$ . Most naturally occurring media (e.g. dielectrics) have both  $\epsilon$  and  $\mu$  greater than zero; however, in certain frequency regimes, many plasmas exhibit permittivity less than zero and permeability greater than zero ( $\epsilon < 0$ ,  $\mu > 0$ ). For example, noble metals (e.g. silver, gold) behave in this manner in the infrared and visible frequency domains. In the other hand, in certain frequency regimes, some gyrotropic materials exhibit permittivity greater than zero and permeability less than zero ( $\epsilon > 0$ ,  $\mu < 0$ ). Artificial materials have been constructed that also have any of these three properties. A medium with both permittivity and permeability less than zero ( $\epsilon < 0$ ,  $\mu < 0$ ), a LHM, has only been demonstrated with artificial constructs. This medium classification can be graphically illustrated as shown in Figure 1.1.

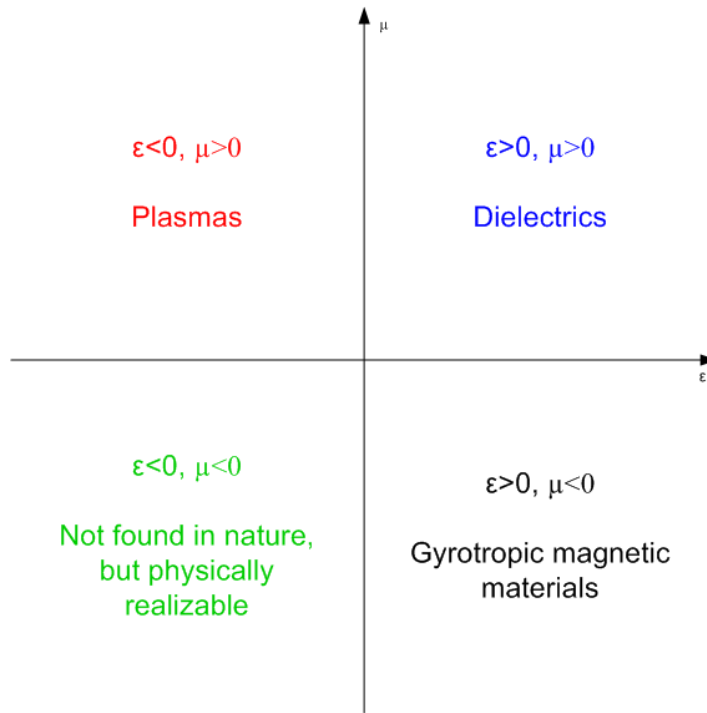


**Figure 1.1.- Material Classifications.**

While a material is often described by some constant (frequency independent) value of the permittivity and permeability, in reality all material properties are frequency dependent. There are several material models that have been constructed to explain the frequency response of materials. One of the most well-known material models is the Lorentz model. It is derived by a description of the electron motion in terms of a driven, damped harmonic oscillator. The Lorentz model then describes the temporal response of a component of the polarization field of the medium to the same component of the electric field as:

$$\frac{d^2}{dt^2} P_i + \Gamma_L \frac{d}{dt} P_i + \omega_0^2 P_i = \varepsilon_0 \chi_L E_i \quad (1.1)$$

The first term on the left accounts for the acceleration of the charges, the second accounts for the damping mechanisms of the system with damping coefficient  $\Gamma_L$ , and the third accounts for the restoring forces with the characteristic frequency  $f_0 = \omega_0/2\pi$ . The driving term exhibits a coupling coefficient  $\chi_L$ . The response in the frequency domain, assuming the  $\exp(+j\omega t)$  time dependence, is given by:

$$P_i(\omega) = \frac{\chi_L}{-\omega^2 + j\Gamma_L\omega + \omega_0^2} \varepsilon_0 E_i(\omega) \quad (1.2)$$

With small losses  $\Gamma_L/\omega_0 \ll 1$  the response is clearly resonant at the natural frequency  $f_0$ . The polarization and electric fields are related to the electric susceptibility as:

$$\chi_{e,Lorentz}(\omega) = \frac{\chi_L}{-\omega^2 + j\Gamma_L\omega + \omega_0^2} \quad (1.3)$$

The permittivity is then obtained immediately as  $\varepsilon_{Lorentz}(\omega) = \varepsilon_0[1 + \chi_{e,Lorentz}(\omega)]$ .

There are several well-known special cases of the Lorentz model. When the acceleration term is small in comparison to the others, one obtains the Debye model:

$$\begin{aligned} \Gamma_d \frac{d}{dt} P_i + \omega_0^2 P_i &= \varepsilon_0 \chi_d E_i \\ \chi_{e,Debye}(\omega) &= \frac{\chi_d}{j\Gamma_d\omega + \omega_0^2} \end{aligned} \quad (1.4)$$

When the restoring force is negligible, one obtains the Drude model:

$$\frac{d^2}{dt^2} P_i + \Gamma_D \frac{d}{dt} P_i = \varepsilon_0 \chi_D E_i \quad (1.5)$$

$$\chi_{e,Drude}(\omega) = \frac{\chi_D}{-\omega^2 + j\Gamma_D \omega}$$

where the coupling coefficient is generally represented by the plasma frequency  $\chi_D = \omega_p^2$ . In all of these models, the high-frequency limit reduces the permittivity to that of free space.

Assuming that the coupling coefficient is positive then only the Lorentz and the Drude models can produce negative permittivities. Similar magnetic response models follow immediately by corresponding the magnetization field components  $M_i$  and the magnetic susceptibility  $\chi_m$ . The permeability is given as  $\mu(\omega) = \mu_0[1 + \chi_m(\omega)]$ .

Metamaterials have necessitated the introduction of generalizations of these models. For instance, the most general second-order model that has been introduced for MTM studies is the two-time-derivative Lorentz Metamaterial (2TDLM) model [17].

## 1.1 Volumetric Left-Handed Metamaterials

A Volumetric LHM is compound of small cubes that are stacked in all directions taking the shape of a bigger cube or a brick. Each small cube is known as unit cell and contains one entire set of inclusions that, when repeated, create the composite media. When many

unit cells have been put together, the LHM looks like a medium synthesized by means of two structures: a thin-wire structure and a Split Ring Resonator (SRR) lattice. Finally the Volumetric LHM can be cut to obtain any shape such as a cylinder or a wedge, provided that the dimensions of the shapes are much bigger than the one of the unit cell. Since the work presented along this thesis is referred exclusively to Volumetric LHMs, they will be called simply LHMs, but the reader must keep in mind its whole meaning.

Idealized LHM is linear, homogeneous, isotropic and non-dispersive three-dimensional structure. In practice, such a material is very difficult to manufacture (in fact, a non-dispersive LHM is impossible because it is not even causal [16]) because of the complexity when it comes to etching a three dimensional shape. A process of construction like this may be very involving and require high technology procedures that are beyond the scope of this work. Instead, the present work deals with two-dimensional structures having one-dimensional responses only; nevertheless, the same concept can be easily translated to a three-dimensional environment by repeating the proposed unit cell, which is just over one coordinate plane, over the other two planes. The one-dimensional response unit cell is made of one either circular or square SRR which is shown to exhibit a negative permeability for frequencies close its the magnetic resonance frequency [14], and one thin-wire since its dielectric permittivity is less than zero below plasma frequency [13] (Figure 1.2a); three-dimensional response unit cell would possess three of each one (Figure 1.2b). One should not mix up the concepts “structure’s dimensions” and “response’s dimensions”; the former refers to number of dimensions the unit cell physically has, while the latter refers to the number of dimensions in which the MTM has

left-handed properties. For example, a one-dimensional response MTM will have left-handed properties only for an incident linearly polarized plane wave; however the unit cell physically has two dimensions. In order to have a left-handed response for a circularly polarized wave, it would be necessary to have a two-dimensional response LHM because circular polarization implies two dimensions.

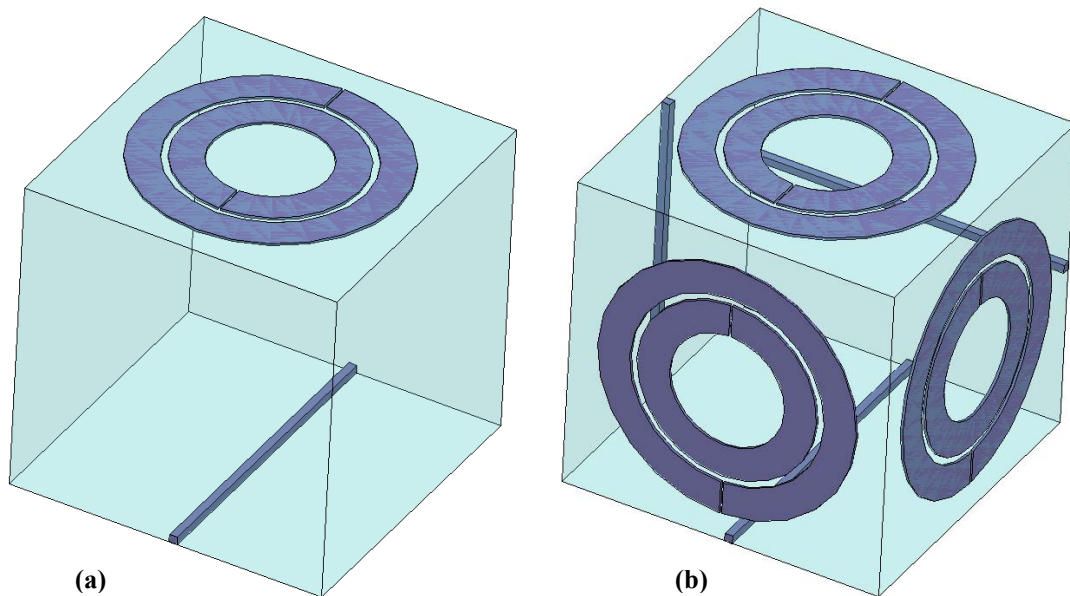


**Figure 1.2.- (a) One-dimensional response unit cell (circular SRR). (b) Three-dimensional response unit cell (circular SRRs).**

For a one-dimensional response MTM, the thin-wire structure is nothing but a simple array of parallel wires set up in the same direction (Figure 1.3). Negative  $\epsilon$  can be obtained from them for all frequencies smaller than plasma frequency  $\omega_p$ , provided that the electric field of the EM wave is polarized parallel to the wires.

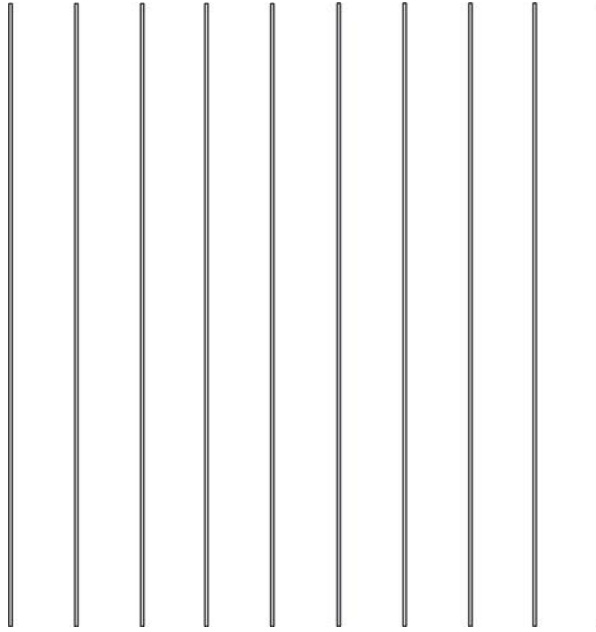


**Figure 1.3.- One-dimensional response thin-wire structure.**

Theory and derivations of the relations that dominate the behavior of the thin-wire structures, formally called “Extremely Low Frequency Plasmons in Metallic Mesostructures”, can be found in [13]. Here only the most important results will be shown and briefly explained.

As in plasma physics, the plasma frequency value and the plasmon’s dielectric function are given by:

$$\begin{aligned}\omega_p &= \sqrt{\frac{ne^2}{\epsilon_0 m}} \\ \epsilon(\omega) &= 1 - \frac{\omega_p^2}{\omega(\omega + i\gamma)}\end{aligned}\tag{1.6}$$

where  $n$  is density of electrons,  $e$  is the electric charge,  $m$  is the mass of the electron, and  $\gamma$  is a damping coefficient. For the case of interest,  $n$  and  $m$  values must be replaced by their effective values, finally the plasma frequency is:

$$\omega_p = \sqrt{\frac{2\pi c_0^2}{a^2 \ln(a/r)}} \quad (1.7)$$

where  $a$  is the separation of the wires and  $r$  is the wire's diameter.

For a one-dimensional response MTM, a SRR lattice (Figure 1.4) provides the negative permeability but, unlike the thin-wire structure, the negative permeability only occurs in a narrow frequency band, on the high-frequency side of the SRR's resonance. This resonance, therefore, determines the range where the material will simultaneously have negative  $\epsilon$  and  $\mu$ , and exhibit a left-handed behavior. In the narrow frequency for which both these parameters are negative, the index of refraction has negative value and the group and phase velocities within the material are anti-parallel.

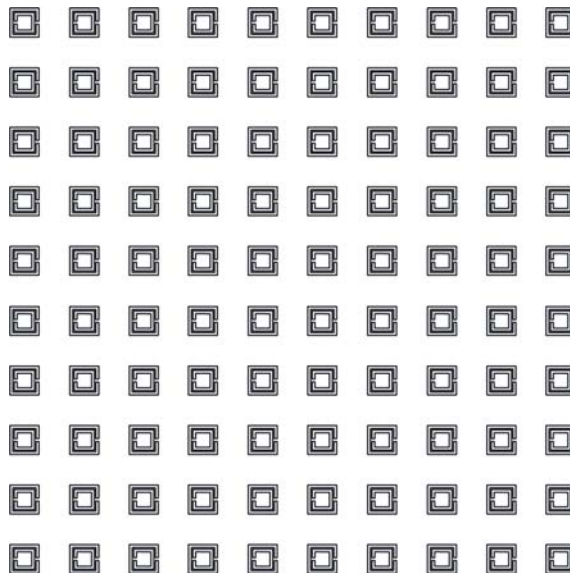


**Figure 1.4.- One-dimensional response SRR lattice (square-shaped SRRs).**

A typical SRR is made of two concentric rings, each interrupted by a small split (Figure 1.5). This split strongly decreases the resonance frequency of the system. Like this, it is possible to obtain a resonant structure with dimensions only a tenth of the corresponding wavelength, compared to a quarter of wavelength for a closed, uninterrupted ring. The scale of the SRR should be much smaller than the corresponding wavelength so that the effective medium theory is applicable; if this condition were not obeyed, there would be the possibility that internal structure of the medium could diffract as well as refract radiation spoiling the phenomenon immediately.

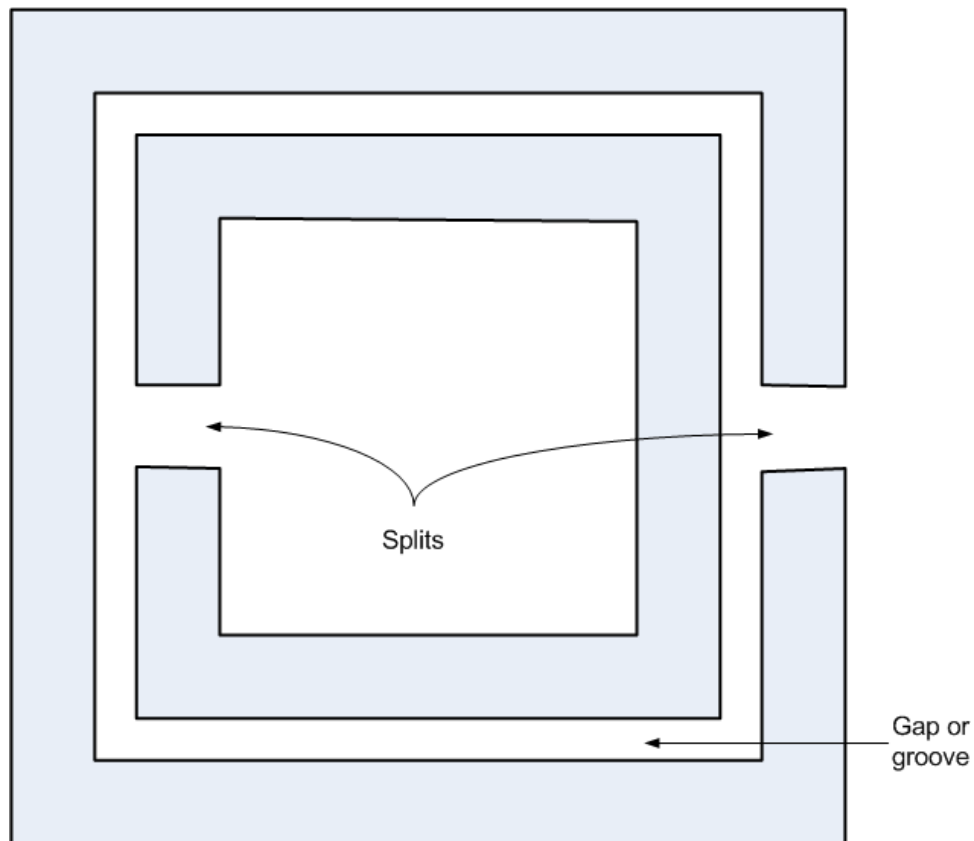


**Figure 1.5.- Typical square-shaped SRR.**

The original SRRs proposed by Pendry (Figure 1.6) were not square but circular rings, nevertheless, rough approximations for square rings can still be calculated using his formulas. Basic relations for these rings are explained in [14] and can be enumerated as follows.

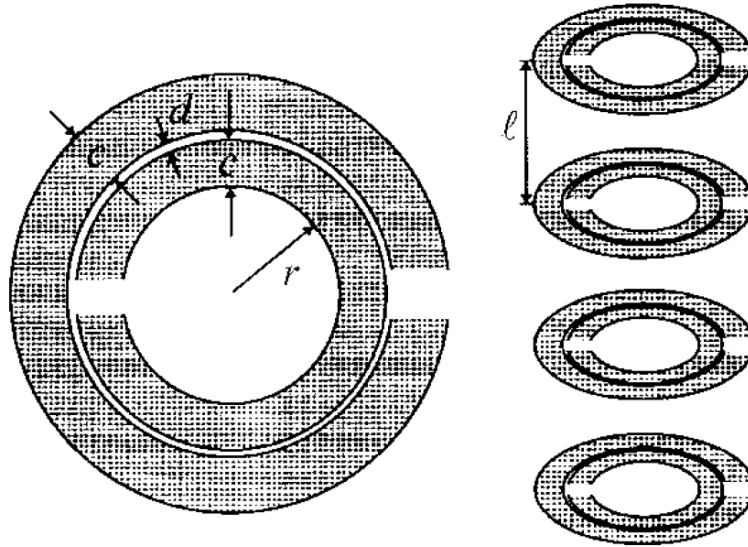


**Figure 1.6. - Left: View of Pendry's SRR showing definition distances. Right: Pendry's SRRs shown in their stacking sequence.**

Assuming,

$$r \gg c, r \gg d, l < r, \ln(c/d) \gg \pi \quad (1.8)$$

the capacitance per unit of length of two parallel sections of metallic strips is:

$$C = \frac{1}{\pi\mu_0 c_0^2} \ln\left(\frac{2c}{d}\right) \quad (1.9)$$

and the effective permittivity:

$$\mu_{\text{eff}} = 1 - \frac{\frac{\pi r^2}{a^2}}{1 + \frac{2l\sigma}{\omega r \mu_0} i - \frac{3lc_0^2}{\pi \ln(\frac{2c}{d})r^3}} \quad (1.10)$$

where  $\sigma$  is the resistivity of the rings.

The most important value, the resonance frequency, is give by:

$$\omega_0 = \sqrt{\frac{3lc_0^2}{\pi \ln(\frac{2c}{d})r^3}} \quad (1.11)$$

From (1.11), it is evident that the strongest parameter that determines the resonance is the value of the radius,  $r$ , which is directly related to the size of the rings. The bigger the ring's size is, the smaller its resonance frequency. The axial separation between rings,  $l$ , is the second most important parameter while  $c$  and  $d$  might be used just for fine tuning.

## 1.2 Bandwidth enhancement

One of the main problems one faces when trying to use a volumetric LHM for a practical application is its lack of bandwidth. Since the pass band is a product of the SRR's resonance, the LHM is essentially a narrow band medium with -3dB transmission bands of around 100MHz [18] [19] [20].

To achieve the goal of improving the way classic volumetric LHMs perform, two approaches are proposed to enhance (increase) their operational frequencies: Varying the size of SRRs and distributing them throughout the unit cell following the Sierpiński

carpet fractal pattern, and the addition of a capability called reconfigurability that allows one to change the shape of the SRRs by connecting or disconnecting each ring.

### **1.2.1 Sierpiński carpet fractal pattern**

According to [21], the Sierpiński carpet fractal (Figure 1.7) is defined as follows:

“The Sierpiński carpet is a plane fractal first described by Waclaw Sierpiński in 1916. The carpet is a generalization of the Cantor set to two dimensions (another is Cantor dust). Sierpiński demonstrated that this fractal is a universal curve, in that any possible one-dimensional graph, projected onto the two-dimensional plane, is homeomorphic to a subset of the Sierpinski carpet. For curves that cannot be drawn on a 2D surface without self-intersections, the corresponding universal curve is the Menger sponge, a higher-dimensional generalization. (...) The construction of the Sierpinski carpet begins with a square. The square is cut into 9 congruent subsquares in a 3-by-3 grid, and the central subsquare is removed. The same procedure is then applied recursively to the remaining 8 subsquares, *ad infinitum*”

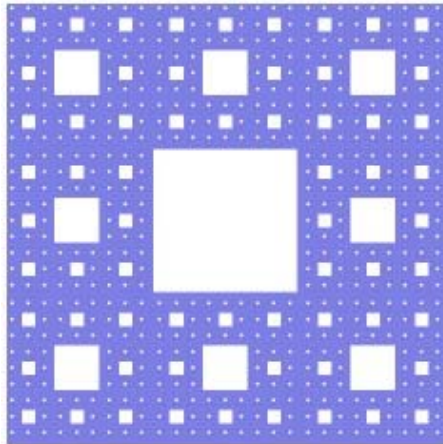


**Figure 1.7.- Sierpinski carpet.**

This pattern was chosen because it provides a great amount of periodicity that is an important requirement for a MTM and, no less important, provides the least amount of disorder which is a crucial feature when designing MTMs [18]. A new parameter can be introduced to account for the amount of disparity inherent to the pattern; this parameter will be called D and it gives a ratio of disparity between a perfectly periodic structure and the “fractal periodicity”.

Values of D are calculated for the first three orders (sizes) of subsquares within a unit cell and a formula is developed for a general nth order.

1 <sup>st</sup> order sub square:	$D_1 = 1 - 1/1$	=0%
2 <sup>nd</sup> order subsquares:	$D_2 = 1 - 8/9$	=11.1%
3 <sup>rd</sup> order subsquares:	$D_3 = 1 - 64/81$	=21.0%
n <sup>th</sup> order subsquares:	$D_n = 1 - (8/9)^{n-1}$	

Simulations showed that only values of disparity below 25% present strong resonances and, therefore, high transmission coefficients  $S_{21}$  ( $>-10\text{dB}$ ). Even though higher values of disparity offer broader bandwidths, the transmission is lousy and only very weak signals can be picked up at the receiving port.

Due to the limitations for the etching process of the available facilities, just the first and second order subsquares will be etched, expecting to have to strong resonances at two different frequencies. The actual resonance frequencies will be design based on other criteria that will be explained in Chapter 2.

### **1.2.2 Reconfigurability**

Reconfigurability denotes the ability of a device or system to be configured, programmed and reprogrammed and whose functionality can be changed during execution. Adding this feature to a MTM does not increase the bandwidth directly, but it enables shifts in the structure's pass band, letting the MTM operate at different frequencies in several moments. This feature enhances the flexibility and frequency agility of the MTM.

To get a reconfigurable MTM, additional splits can be cut in both the internal and external rings and switches can be placed over these splits so they can connect and disconnect the arms of each ring (Figure 1.8). By doing this, different configurations or shapes of SRRs are achieved and different responses are obtained [22]. An intrinsic

problem of this approach is the biasing of the switches. A great number of lines would be needed to control each switch and they might interfere with the overall performance of the MTM. Instead, some MEM switches can be biased by applying strong static electric fields [23] [24], which is a more promising way to control the MTM's response without affecting its operation. Alternatively, photosensitive semiconductors might fill the splits in such a way that each split in the unit cell responds to a certain wavelength, then having a transparent dielectric host material, the photosensitive switches can be easily controlled by light.

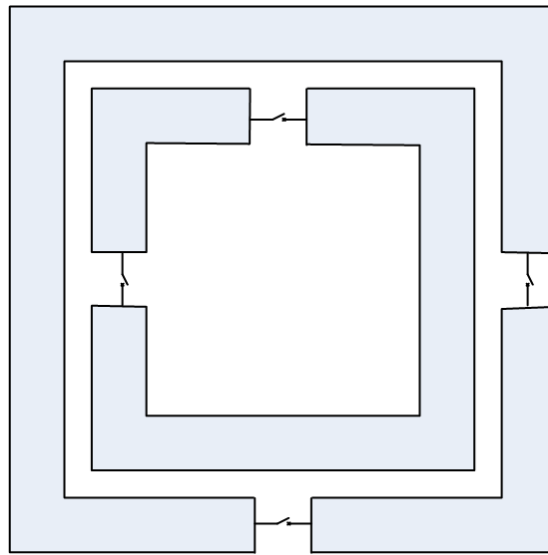


**Figure 1.8.- Diagram of a Reconfigurable SRR.**

Throughout this thesis, simulations are performed by either opening or short-circuiting the gap. Building and testing this reconfigurable structure is left as future work.

## **CHAPTER 2**

### **DESIGN & SIMULATION**

The lack of exact formulas that describe the EM behavior of the inclusions inside a LHM make the design & simulation processes become even more closely related than usual. For this reason simulations are usually the only way to test a change in any dimension of an inclusion. From formulas, one can qualitatively anticipate, for example, whether the resonance will shift up or down in frequency, but it will be hard to know the exact shifting with a reasonable accuracy. The design process, therefore, requires a continuous iteration of simulations to achieve the needed response at the desired value.

The MTM's models were simulated using ANSOFT's High Frequency Structure Simulator (HFSS) v11. HFSS is commercial finite element method (FEM) solver for electromagnetic structures; it is one of the most popular and powerful applications used for antenna design and the design of complex RF electronic circuit elements including filters, transmission lines, and packaging. FEM is a numerical technique for finding approximate solutions of partial differential equations (PDE) as well as of integral equations. The solution approach is based either on eliminating the differential equation completely (steady state problems), or rendering the PDE into an approximate system of ordinary differential equations, which are then solved using standard techniques. The most advantageous feature of this method is its ability to handle complex geometries and boundaries, which are very common in MTM structures, with relative ease.

This chapter has been divided in five parts: The first one explains the methodology used in HFSS to create a linearly-polarized plane wave, the ports' integration line and a special boundary condition (BC) called Master/Slave BC that is useful for periodic structures. The second part talks about the most crucial and delicate part of the design which is the design of the reconfigurable SRRs in its two sizes; ideas like predicting resonance shifts when varying certain SRR's dimensions, identifying the resonances and changing the switches' state will be clarified. The third part is focused in arranging the SRRs according to the Sierpiński-carpet fractal distribution and emphasizes the double magnetic resonance of the structure and their values. The fourth one gives details about the thin-wire structure and the plasma frequency it needs to have in order to have a good trade off between attenuation and negative permittivity. Finally in the fifth section, both components (wires and SRRs) are put combined and the overall response is obtained.

## **2.1 Plane wave port generation and Master/Slave boundary conditions**

The first step in setting up a simulation for the one-dimensional response LHM in HFSS is the correct generation of the incident wave for the reason that it needs to be a monochromatic uniform linearly-polarized plane-wave, otherwise only part of the wave will be affected by the LHM, or the LHM's effect can be inhomogeneous leading to erroneous results. To fulfill these requirements, the generated wave must have its electric and magnetic fields always perpendicular to the direction of propagation (TEM wave)

and furthermore, each field must be parallel to a coordinate axis at every single point within the space the wave is propagating while having no attenuation or losses inside that space. A plane wave can be easily generated by assigning a plane-wave excitation to a face; however, this kind of excitation is not a port and does not allow the measurement of the reflection and transmission (S-parameters) which is the ultimate goal. The appropriate configuration is shown in Fig 2.1, where a port is defined in a rectangular face of the model (transmitter face); two opposite faces adjacent to the transmitter face are set as Perfect Electric Conductors (PEC) and the other two are set as Perfect Magnetic Conductors (PMC). By doing this, the electric field lines are forced to be parallel to the PMC walls but perpendicular to the PEC walls, while the magnetic field lines are forced to be parallel to the PEC walls and perpendicular to the PMC walls resulting in the required plane wave.

The port's integration line is a vector that represents both a calibration line that specifies the direction of the excitation electric field pattern at the port and a line along which to compute the port's impedance. For the plane-wave case in consideration, the integration line is a straight line from one PEC face to the other one; this line coincides with an electric field line of force which is the red arrow in Figure 2.1.

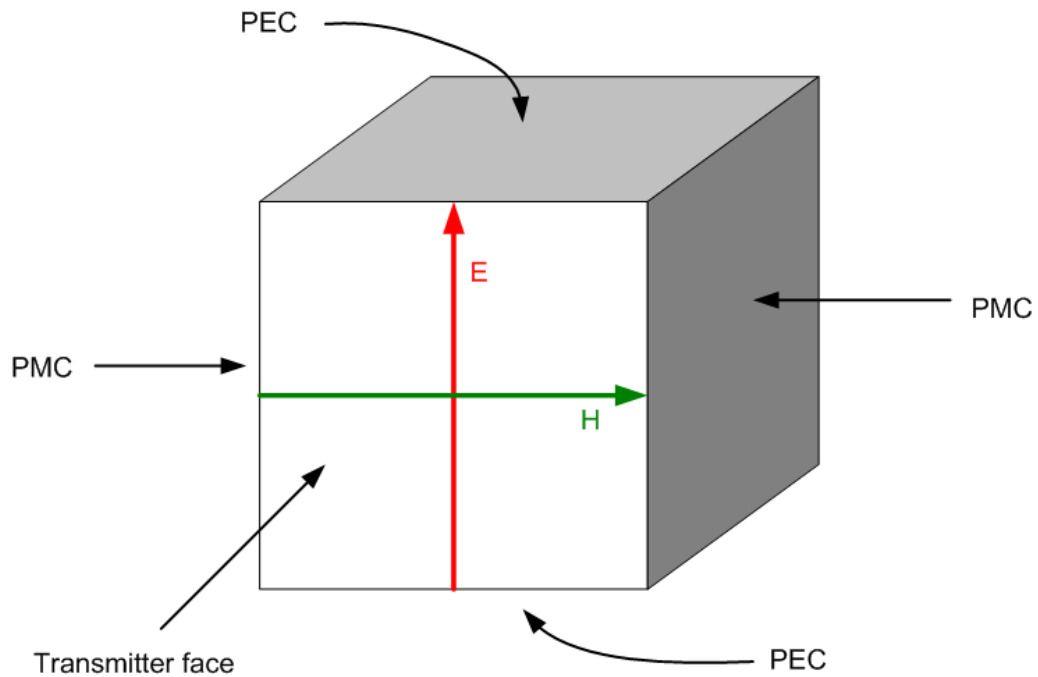


**Figure 2.1.- Plane wave generation arrangement.**

Master/slave boundaries enable modeling periodic planes where the electric field on one surface matches the electric field on another one with a phase difference. They force the electric fields at each point to be the same at both master and slave faces. They are useful for simulating infinite periodic structures. Master/slave BCs facilitates the simulation of MTMs that are infinitely long in two dimensions. It means that the MTM can contain an infinite number of unit cells throughout the wave front plane which is the plane where the E and H fields lie or, since it is a uniform plane wave, the plane perpendicular to the direction of propagation. This BC conveniently removes fringing effects and edge diffractions of finite structures. Along the direction of propagation a finite number of unit cells can be placed which represents the thickness of the MTM.

Figure 2.2 shows an example of the implementation using the plane-wave generation arrangement and the master/slave BCs. A unit cell of LHM is surrounded by two pairs of master/slave boundaries, where the top face matches the bottom one, and the left face matches the right one. Finally a plane wave generation arrangement is placed at the front face and another one at the back face of the unit cell. In this manner, a plane-wave impinging on an infinitely long slab of LHM can be simulated and its transmission and reflection S-parameters can be computed using the front and back ports.

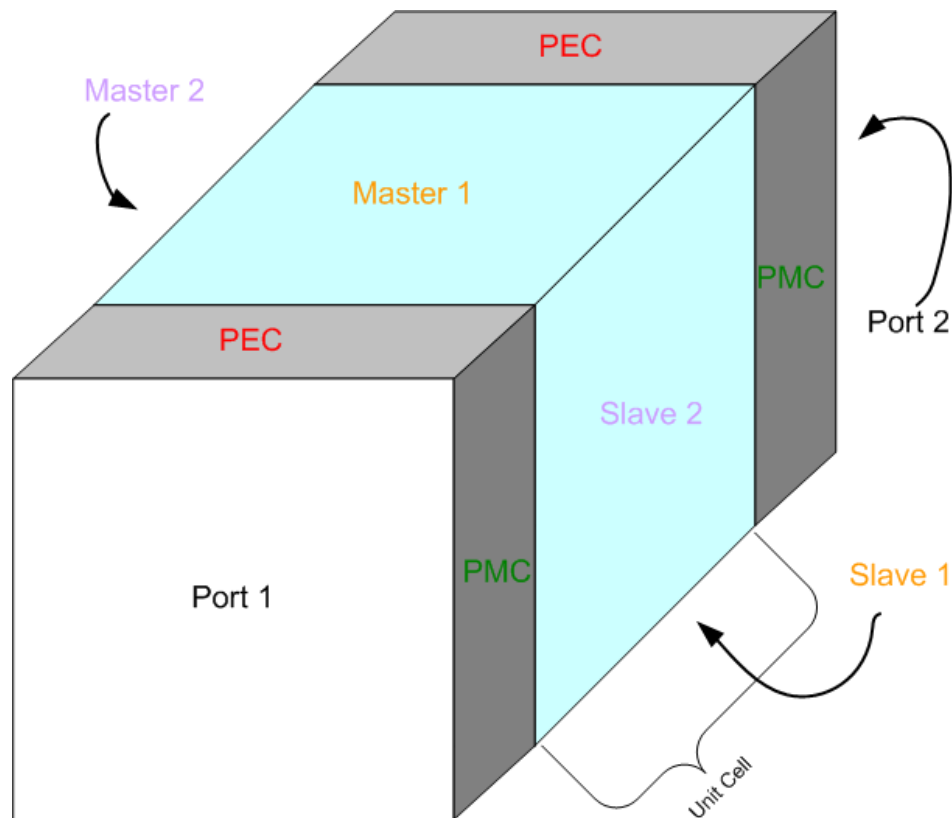
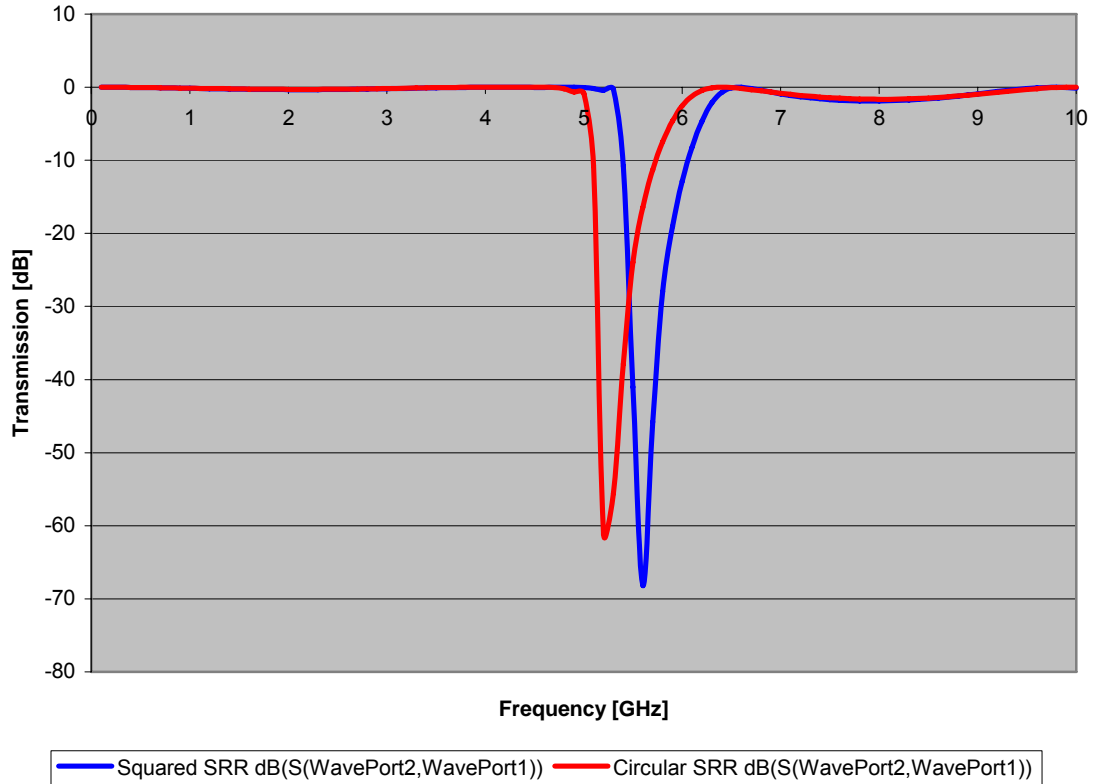


Figure 2.2.- Simulation boundary conditions setup.

## 2.2 Reconfigurable SRR design and simulation

In general, researchers have worked with two well known SRR shapes: circular and square-shaped ones (Figures 1.6 and 1.5, respectively). Both resonate at certain frequencies at which SRRs behave like a filter reflecting all the incident power back to the transmitter. Furthermore, both rings have almost the same response over the band of interest, though at higher frequencies some electric resonances appear for the square-shaped SRR but not for the circular one. Figure 2.3 shows a comparison over the band of interest between the two SRRs designed for almost the same resonance frequency. The circular SRR's response is shown in red and the square-shaped SRR's response is shown in blue. Only small discrepancies can be found between the two responses. At resonance, all the power is reflected and, for all other frequencies, SRRs behave as if they were not physically present since all the power is transmitted. This resonance is known as a magnetic resonance because it is the magnetic field what creates the resonance. Magnetic field lines that cross the rings induce currents on the rings; these currents can only travel around the rings at the resonance frequency because at other frequencies the capacitances of the splits represent large impedances that prevent the currents from flowing. The main characteristic of magnetic resonance is that the wavelength associated with the magnetic resonance frequency is much larger than the structure dimensions [14]. The reason why square SRRs are considered in this work is because they are much easier to fabricate with precision.

Pendry's basic formulas presented in Chapter 1, and concepts presented by Aydin in [18] were very helpful in designing SRRs. The first parameter to be chosen is the size of either the large or the small SRR (length of the external SRR's edge in Figure 1.5); the size of the other one will be determined by the Sierpiński-carpet as will be explained in the following section. The size will approximately define a frequency range of about 1GHz where the resonance will fall. Equation (1.11) is used as a first theoretical approach. Simulations and [25] show that if one stacks unit cells along the direction of propagation, the S-parameters of the entire structure converge when there are around eight unit cells. Having this criterion and taking into account that real substrates come in standard sizes ISO296 [26] such as A4, A3, A2, etc., the proposed size for the large rings is 12.50mm which is about 297mm (the width of the A3 size) divided by 8 (number of unit cells) and divided by 3 (due to the Sierpiński carpet). Consequently, the size of the small rings will be 4.16mm, one third of the largest ring size.



**Figure 2.3.-  $S_{21}$ -parameter for square and circular SRRs.**

The SRR structure has capacitive elements that increase the response of the material to the incident radiation. Capacitance due to splits prevents current from flowing around the rings, but mutual capacitance between the two rings enables the flow of current through the structure [14]; these are the main contributions to the total capacitance of the system. Inductances arise from the conducting rings and the gap between the concentric rings [22]. By changing the dimensions of any of these parts, fine tuning can be performed. The effect of the split width is to change the capacitance of the system. If the split is shortened, the capacitance of the system is increased; therefore the resonance frequency is decreased. The effect of the gap distance between rings is changing the capacitance of

the system as well, so the result is the same: the shorter this gap, the lower the resonance frequency. The ring's width, in the other hand, affects both the capacitance and the inductance of the system [22]. Increasing the metal width will decrease the mutual inductance and mutual capacitance, and thus SRRs made of thinner rings yield lower resonant frequencies.

Reconfigurability with SRRs is achieved by using two reconfigurable splits on each ring. These splits can be closed (short-circuited) by a tiny switch placed across them. Having one split open, when the other one is also opened, a capacitance is added in series to the first one resulting in an effective lower capacitance and higher resonance frequency.

Additionally, one split is twice as wide as the other one; hence their capacitances are one unit and half a unit. When these capacitances are combined, the equivalent capacitances the splits provide can be one unit, half a unit or one third of a unit, when the smaller, the bigger or both splits are open, respectively. Simulations of closed splits are conducted by just leaving the SRR arms intact. That means that no actual switch is placed in the simulation but a split is inserted when an open switch is required and the split is removed when a closed switch is used.

### **2.2.1 Large SRR**

A large SRR was already defined earlier as having edges of 12.50mm. This leaves four distances to determine: the rings' width, the gap's width, the split's length and the separation in the stacking sequence (distance  $l$  in Figure 1.6). Distance  $l$ , which is the

second most important value to use in order to adjust the resonance, is not a free-to-change value because it is the most important parameter used to design the thin-wire structure. Consequently, the combined LHM's design can not be easily broken in two separate designs. On the contrary, both parts are closely related and during the process it is unavoidable to go back and forth to achieve the optimum dimensions. Because of the edge's size, the resonance large SRR's resonance frequency should fall in the G Waveguide Frequency Band (WFB), which covers the spectrum from 3.95 to 5.85GHz. The three sizes left are designed so that the resonance is centered in the G WFB at roughly 5GHz.

After running some HFSS simulations on thin-wire structures (they will be explained in section 2.4) and on SRRs trying to bring their resonance frequency as close to 5GHz as possible, a good compromise between them was found at  $l = 6\text{mm}$ . Thus, using (1.11):

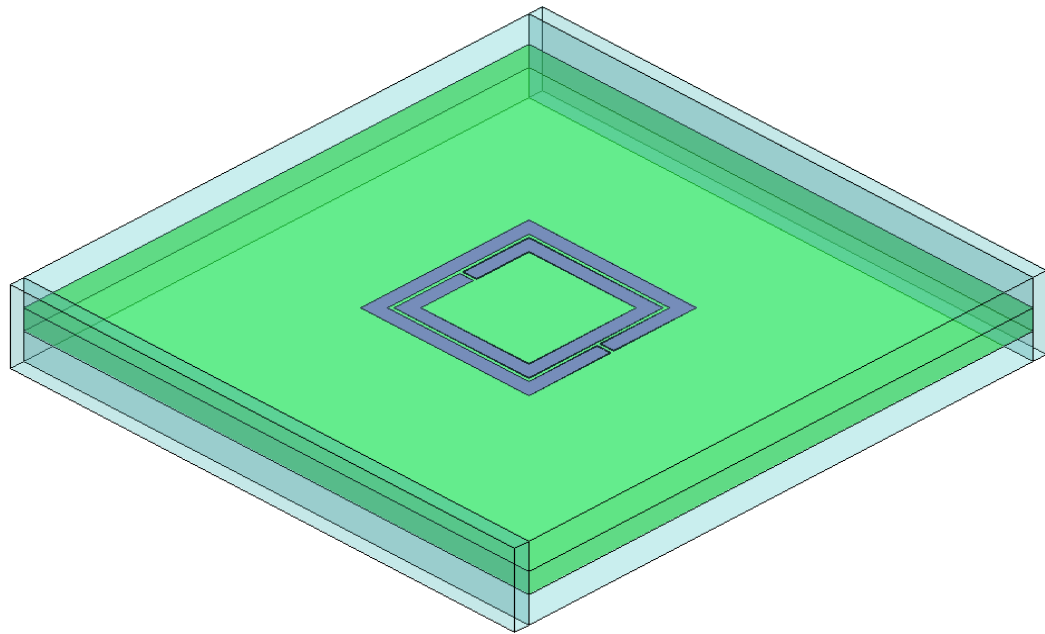
$$2\pi \cdot 5 \cdot 10^9 = \sqrt{\frac{3 \cdot 0.006 \cdot (3 \cdot 10^8)^2}{\pi \ln(2 \frac{c}{d}) 0.00625^3}}$$

$$c / d = 4.25$$

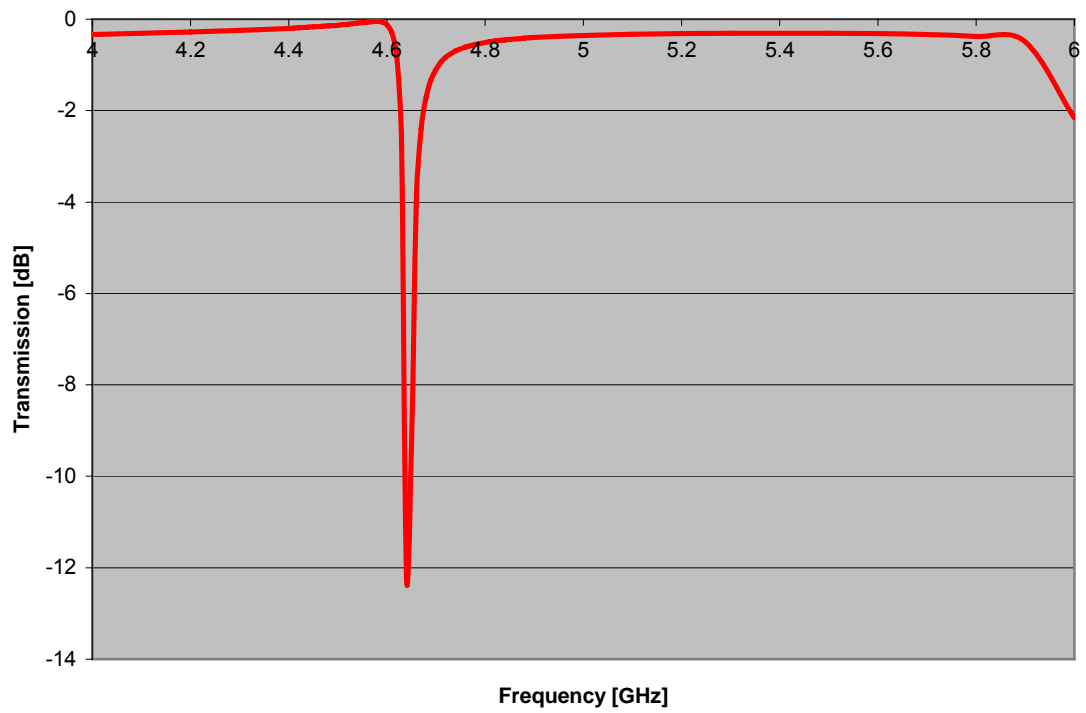
This crude approximation states that the ratio between widths of the ring and the gap is 4.25 and both,  $c$  and  $d$  (Figure 1.6), must be much less than 6.25mm (12.50mm/2). For a first simulation, the diameter of a small drill bit (0.25mm) is chosen as gap width and split length since drill bits will be used to etch them; hence  $c = (4.25)(0.25\text{mm}) \approx 1\text{mm}$  is the ring's width.

A snapshot of the simulation geometry using the values specified above is shown in Figure 2.4a and the computed outcome is shown in Figure 2.4b. The geometry contains a substrate over which the rings are positioned; the substrate's thickness is 1.61mm and its relative permittivity is 2.17. The thickness of the rings is 35 $\mu$ m and they are simulated as PEC. The simulation gives a resonance frequency at 4.64GHz; in order to shift it to 5GHz, one may either increase the split's and gap's length or make the rings wider. After a number of simulations, the resonance frequency is finally relocated at 5.03GHz by dimensioning the rings as depicted in Figure 2.5.

Additional splits are opened to make the SRRs reconfigurable; a split of  $0.25/2 \approx 0.12$ mm is cut from both rings (Figure 2.6). Switches A, B, C and D are defined giving sixteen different possibilities of resonance variation. Excluding the seven configurations that do not have at least one split in each ring (see Table 2.1), and hence do not possess magnetic resonance, nine different resonances can be achieved from this reconfigurability capability. The nine resonance frequencies can be observed in Figure 2.7; they range from 4.08GHz to 6.31GHz and vary in intensity from -8dB to -28dB. An important point to notice is the fact that in general, the resonances are very intense and sharp, giving a resonance bandwidth of only some tens of megahertz; however, the actual bandwidth is slightly broadened when several unit cells are stacked along the direction of propagation; this effect can be examined in the simulations of Appendix A.

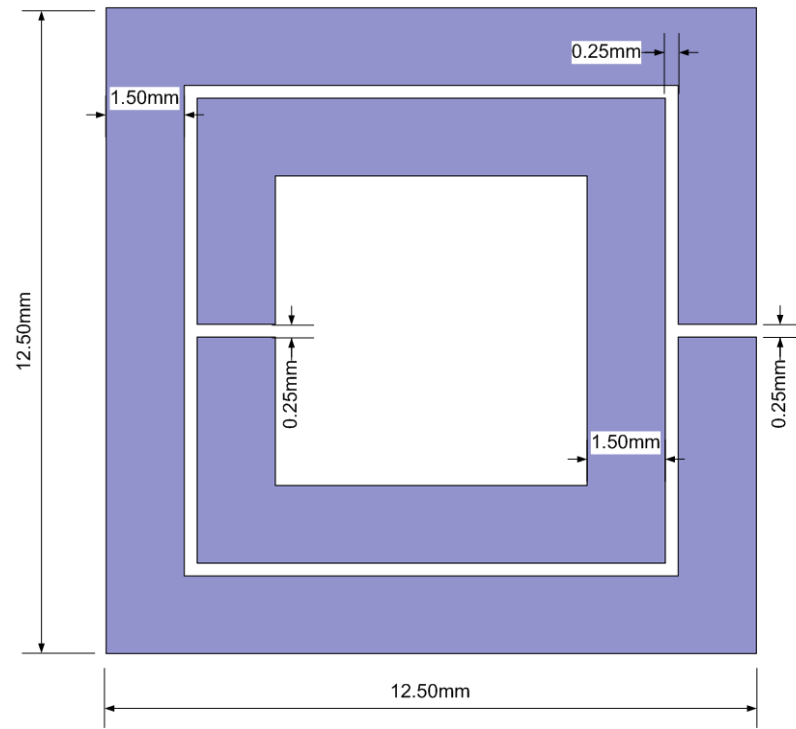


(a)

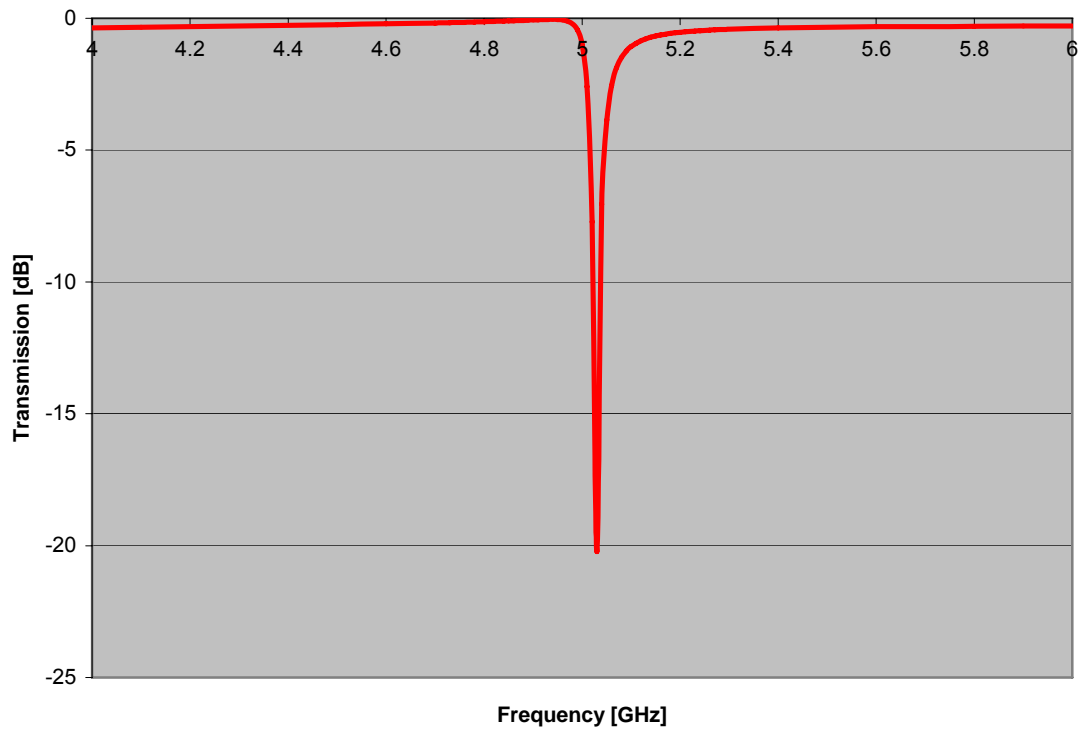


(b)

Figure 2.4.- (a) Snapshot of the first simulation prototype. (b)  $S_{21}$ -parameter of the prototype.



(a)



(b)

Figure 2.5.- (a) Dimensions of the large SRR's final design. (b) Its  $S_{21}$ -parameter.

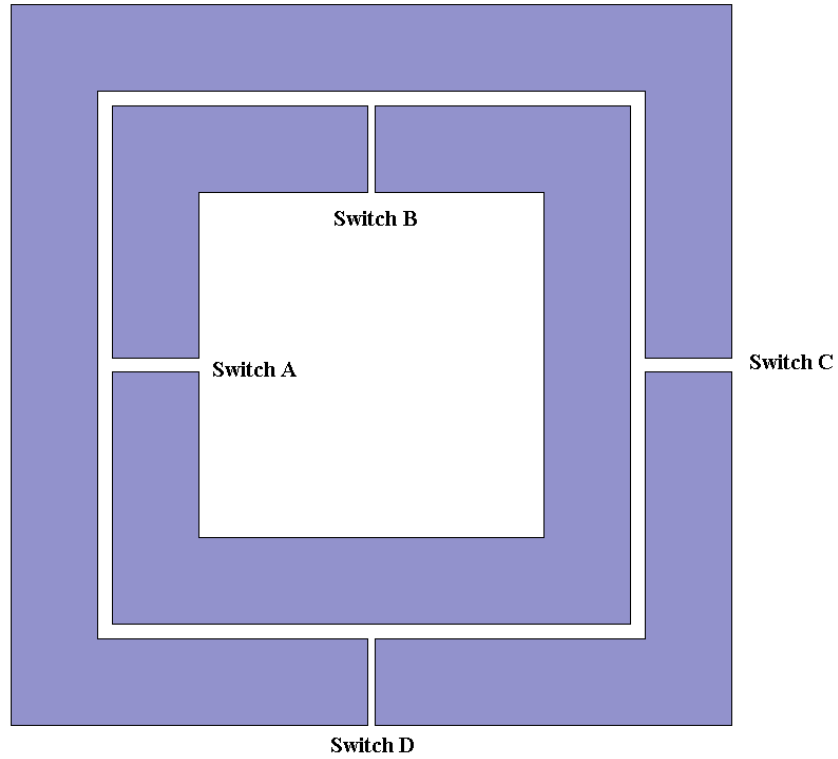
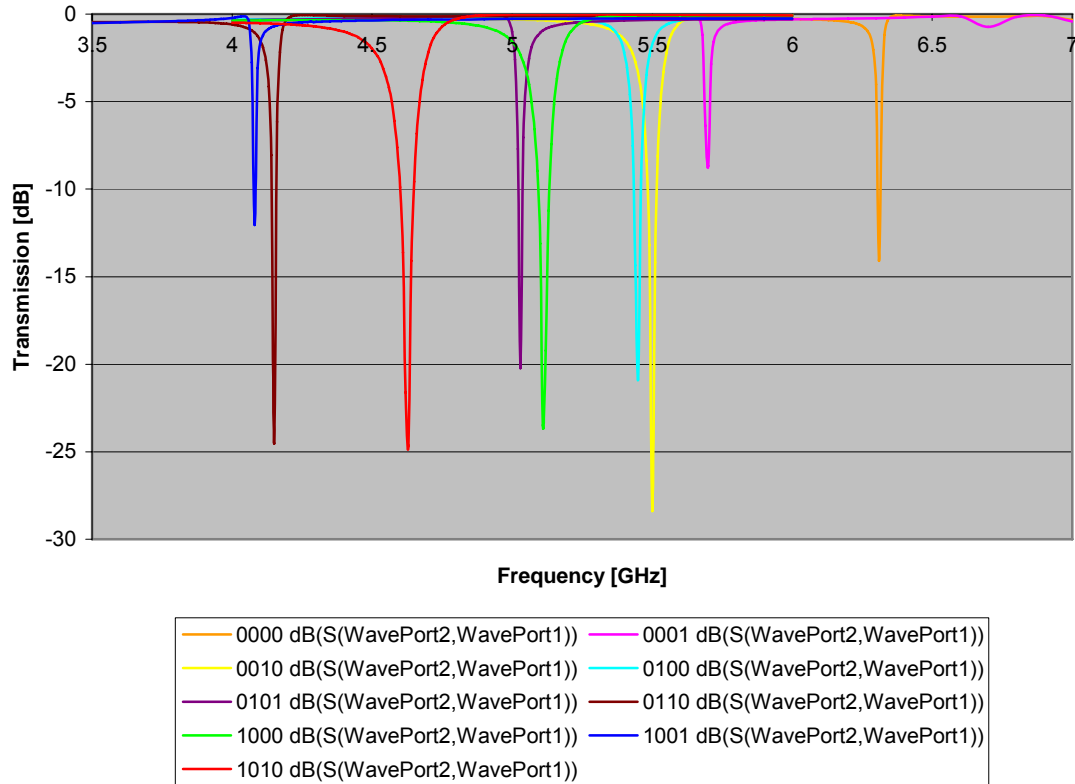


Figure 2.6.- Split switch labels.

A	B	C	D	Resonance Frequency [GHz]
0	0	0	0	6.31
0	0	0	1	5.70
0	0	1	0	5.50
0	0	1	1	-
0	1	0	0	5.45
0	1	0	1	5.03
0	1	1	0	4.15
0	1	1	1	-
1	0	0	0	5.11
1	0	0	1	4.08
1	0	1	0	4.63
1	0	1	1	-
1	1	0	0	-
1	1	0	1	-
1	1	1	0	-
1	1	1	1	-

Table 2.1.- Resonance frequencies for each switch configuration.



**Figure 2.7.- Reconfigurable large SRR resonances.**

### 2.2.2 Small SRR

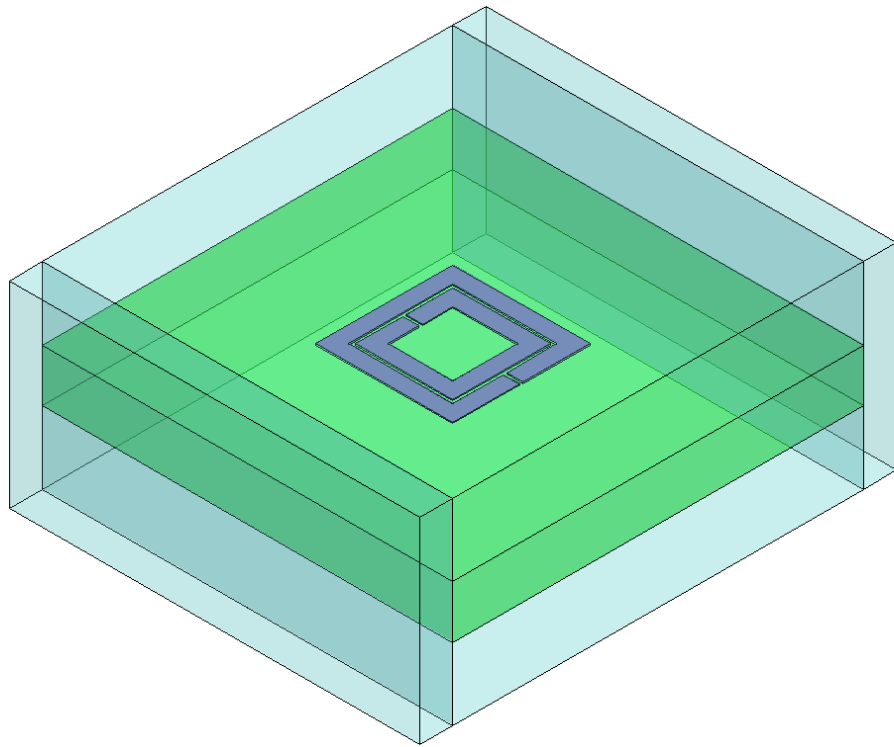
The design procedure of the smaller SRRs is basically the same as the one for the large SRRs. The only huge difference is the fact that the small size imposes technical problems when etching gaps and splits. For this reason, tiny shapes must be carefully designed considering the physical limits of the fabrication process.

A small SRR edge size was defined as 4.16mm and the stacking sequence,  $l$ , as 6mm. Due to its size, the small SRR magnetic resonance frequency can fall in frequencies up to

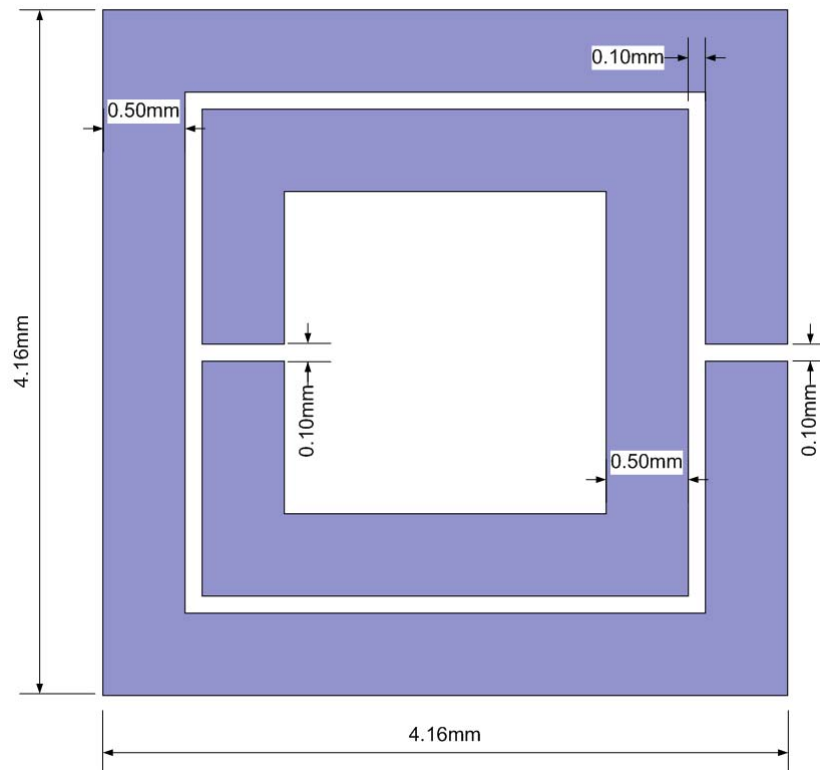
the Ku WFB that covers the EM spectrum from 12.4 to 18GHz. Nevertheless, the small SRRs can also work at lower frequencies. In fact, the lower the frequency, the smaller the inclusions will be compared to a wavelength so the more homogeneous the MTM will be. The only challenge is to achieve a low resonance frequency using such small SRRs. The design's goal is to get a resonance frequency as low as possible so that both small and large reconfigurable SRRs can work at close frequencies. It would allow, for example, having both resonances so close that they would partially overlap, giving a broader effective LHM bandwidth.

Using the criteria describe earlier, the best way to get a low resonance frequency is to make splits, gaps and rings as thin as possible. The mechanical etching process imposes constraints for fabricating small shapes: the current available facilities do not allow making strips narrower than 5mm; as a result, 5mm will be the width of the rings. In the other hand, the thinnest drill bit has a diameter of 0.1mm so it will be the narrowest etching width and, therefore, the gap's and split's width.

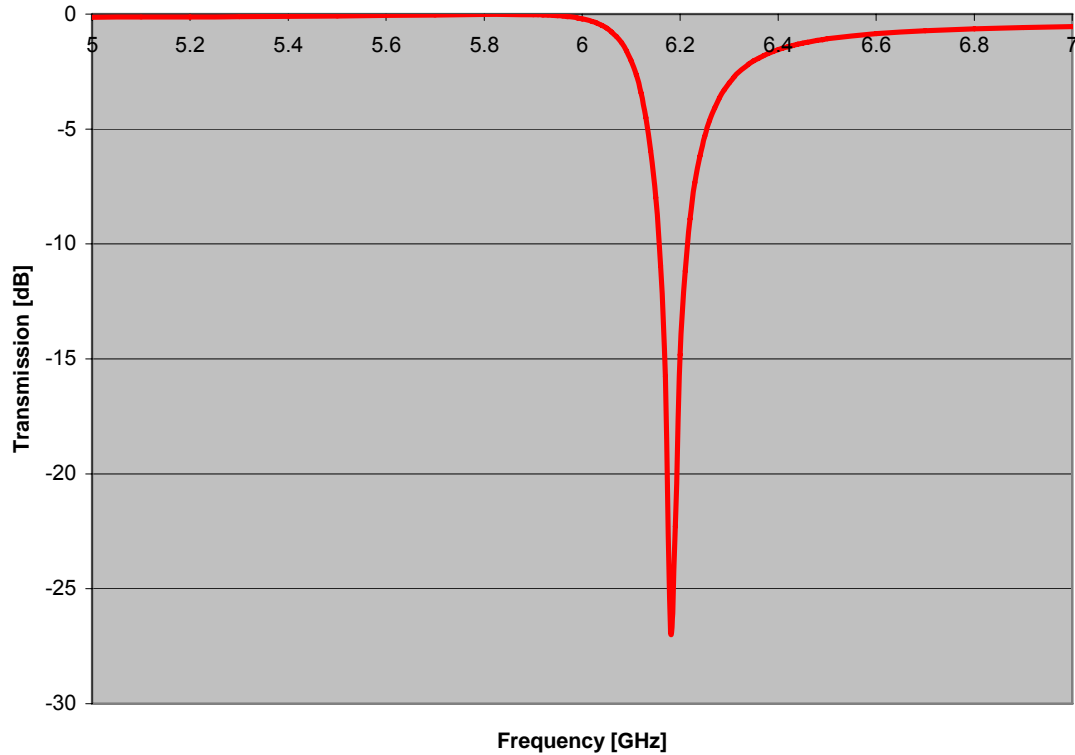
The simulation results from the model using these dimensions, the small SRR's final dimensions and the  $S_{21}$ -parameter are shown in Figure 2.8. The resonance emerges at 6.18GHz which is very close to the highest resonance frequency obtained with the reconfigurable large SRRs, 6.31GHz.



(a)



(b)



(c)

**Figure 2.8.- (a) Snapshot of final small SRR simulation geometry. (b) Dimensions of the small SRR's final design. (c) Small SRR's  $S_{21}$ -parameter.**

Finally, additional splits are inserted to make the small SRR reconfigurable. Only for simulation purposes, a split of  $0.1/2=0.05\text{mm}$  is cut out from both rings in the same fashion as it was done for the large SRRs, and the same labeling is applied. Again, nine magnetic resonance frequencies can be observed for the small SRRs (Figure 2.9), ranging from 5.31GHz to 7.72GHz and varying in intensity from -34.7dB to -21.5dB. The range of frequencies is very close to the one of the large SRRs, thus the objective was successfully accomplished.

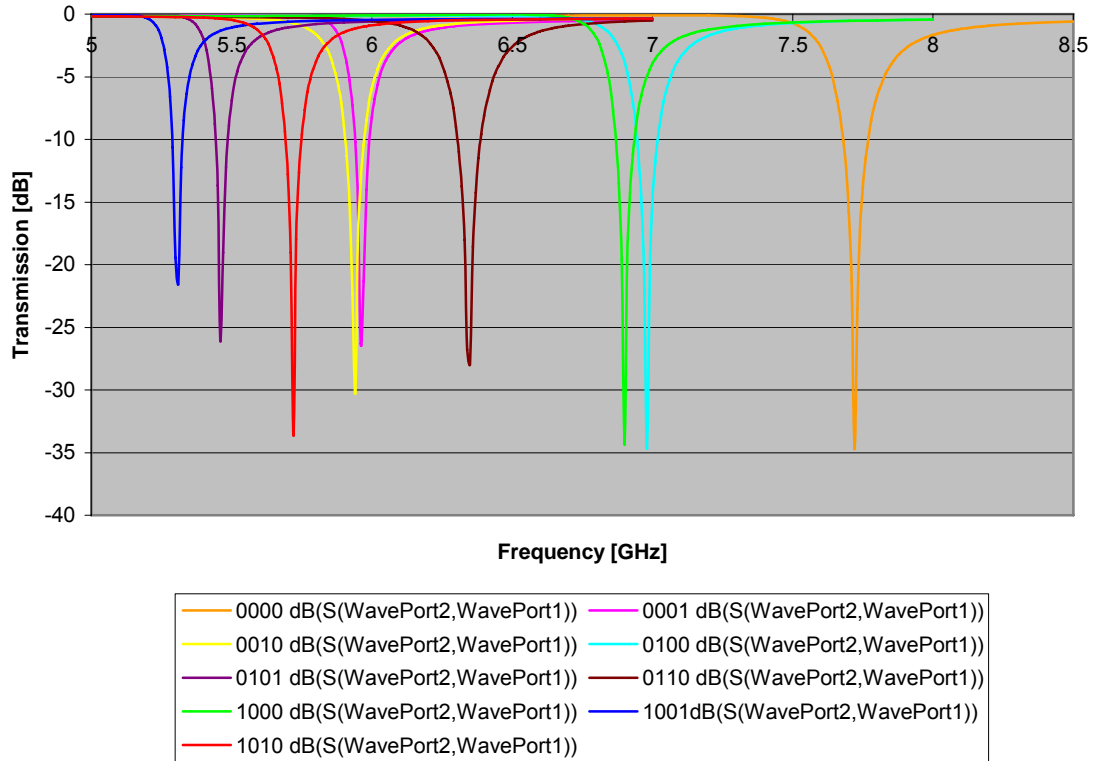


Figure 2.9.- Reconfigurable small SRR resonances.

### 2.3 Sierpiński-carpet-arranged SRRs design and simulation

As it was mentioned earlier, large and small SRRs are arranged using the Sierpiński-carpet fractal pattern. Since there are only two sizes, the Sierpiński-carpet is implemented only up to the second order of subsquares, however smaller sizes can be fabricated, but always taking into consideration of the disparity value  $D$ .

A second order Sierpiński-carpet fractal pattern is shown Figure 2.10. The large square's edge is three times longer than the one of the small square. That is the reason why the

sizes of the SRRs were chosen the same way during the design in section 2.2. One thing that might not be evident is how the combined unit cell would look like. The unit cell is the combination of one large SRR and eight small SRRs around the large one, acting like satellites around a planet (Figure 2.10). If a third order pattern were to be implemented, eight smaller satellites would have to be added around each small satellite.

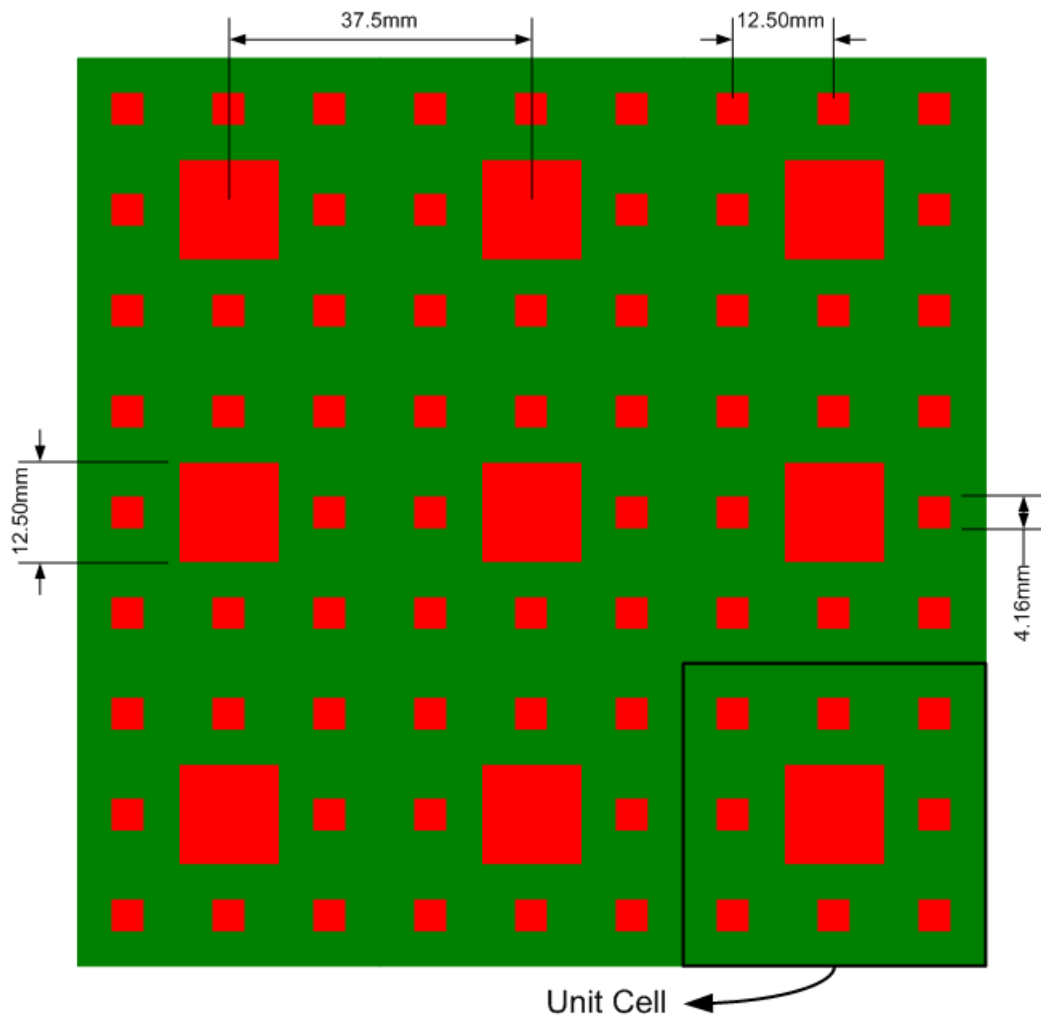
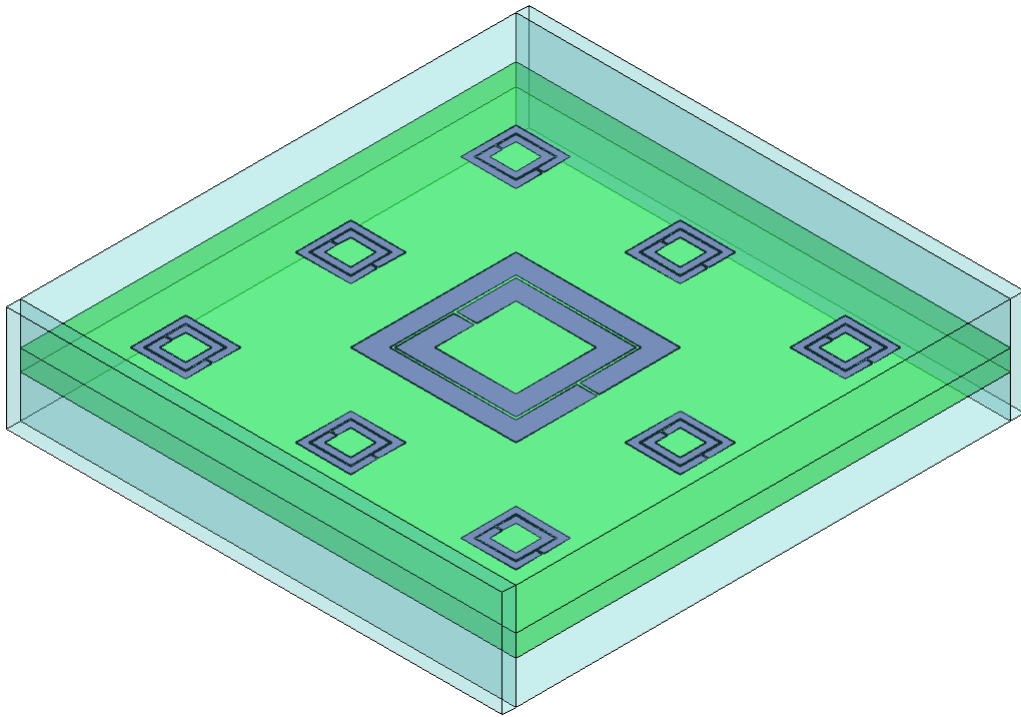


Figure 2.10.- Second order Sierpiński-carpet fractal pattern.

The Sierpiński-carpet-arranged SRR simulation model is presented in Figure 2.11. The model contains one unit cell where the small and large SRRs are the original ones (without adding splits for reconfigurability), and hence two resonances are obtained at 5.03GHz and 6.18GHz.



**Figure 2.11.- Sierpiński-carpet-arranged SRR simulation geometry.**

Computations were performed with the usual boundary conditions setup and the same substrate material used in previous simulations. The results are presented in Figure 2.12. Two resonances appear at 4.89GHz and 6.1GHz, very close to the designed frequencies. Resonance intensity and shape varied compared to the case of individual simulations; this

is expected because, at resonance, the wave is reflected by SRRs of one size, but it is also scattered by the ones of the other size which represent obstacles that prevent the model from having the original strong resonance. Also, less strong resonance are expected at the final simulation for the small SRRs due to its value of disparity.

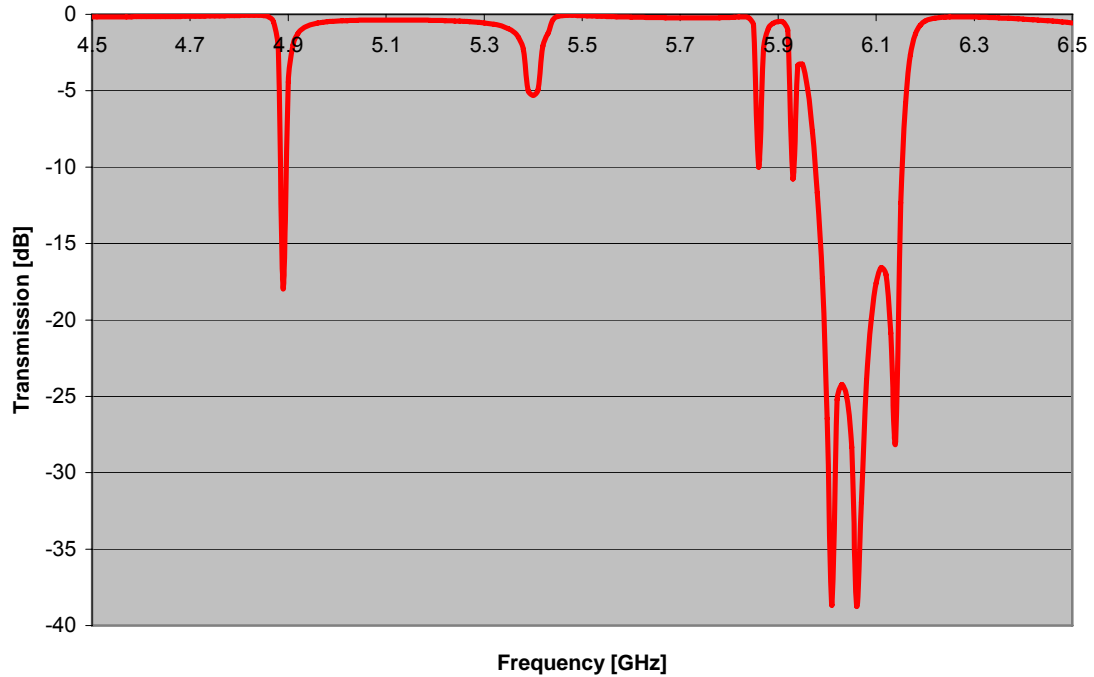


**Figure 2.12.- Sierpiński-carpet-arranged SRRs  $S_{21}$ -parameter.**

At this point, only half of the design is complete: the SRR layer. Two magnetic resonances have been obtained and, to complete the LHM, the thin-wire structure needs to be designed to provide the negative permittivity at the two magnetic SRR resonances.

## 2.4 Thin-wire structure design and simulation

Pendry originally proposed a structure composed of infinite wires arranged in a simple cubic lattice. For a one dimensional response LHM, that structure is a series of parallel wires laying in the same direction of the waves' electric field as shown in Figure 2.13.

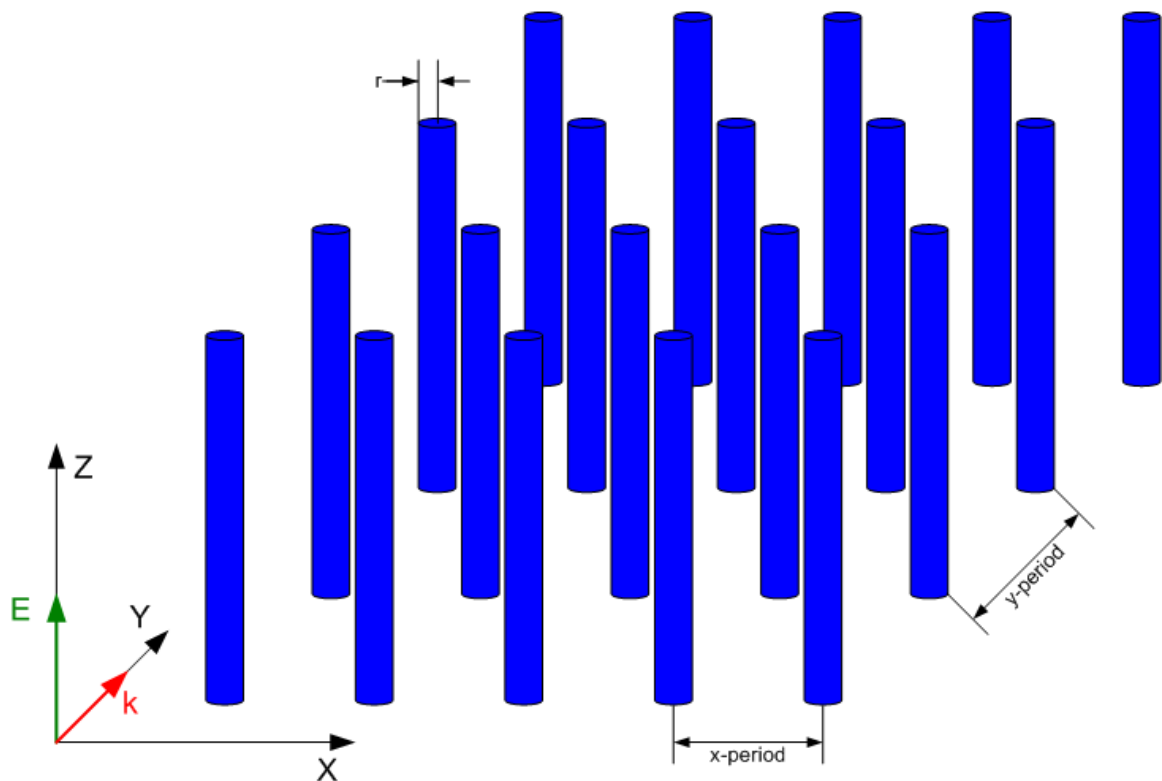


Figure 2.13.- One-dimensional response thin-wire structure.

This structure works as a plasmon which is a well established collective excitation of metals in the visible and near UV frequencies. At much lower frequencies dissipation

destroys all trace of the plasmas and typical Drude behavior sets in. However periodic structures made of thin wires dilute the average concentration of electrons and considerably enhance effective electron mass through self-inductance. This mechanism lowers plasma frequency into the far infrared or gigahertz band.

Actual implementations generally do not allow the same period in both directions, x and y, due to mechanical constraints. The designer has to choose the right periods to obtain the plasma frequency and attenuation. Through simulations of one dimensional response thin-wire structures one can conclude that the plasma frequency is drastically affected by the period in the x direction while the attenuation's slope below the plasma frequency is greatly influenced by the y-period.

Given that the small SRR's resonance frequency is about 6.2GHz, a separation and security margin of 1GHz is added to it to approximate an appropriate plasma frequency for the thin-wire structure. Equation (1.7) is good for predicting the separation of the wires (or x-period):

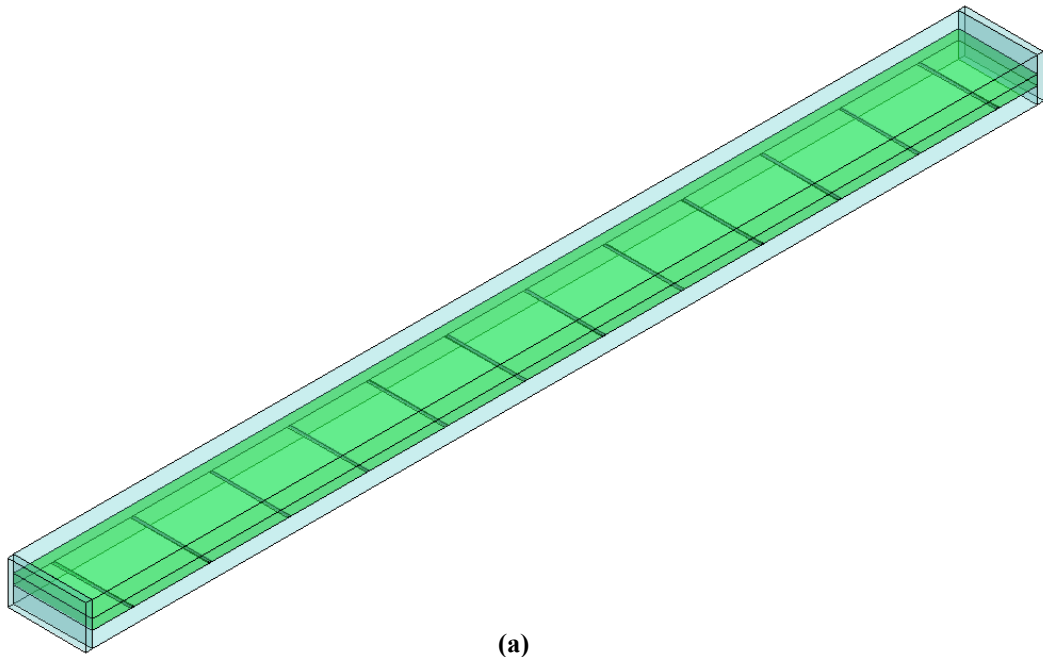
$$2\pi \cdot 7.2 \cdot 10^9 = \sqrt{\frac{2\pi(3 \cdot 10^8)^2}{a^2 \ln\left(\frac{a}{17.5 \cdot 10^{-6}}\right)}}$$

$$a = 6.81 \cdot 10^{-3} m = 6.81 mm$$

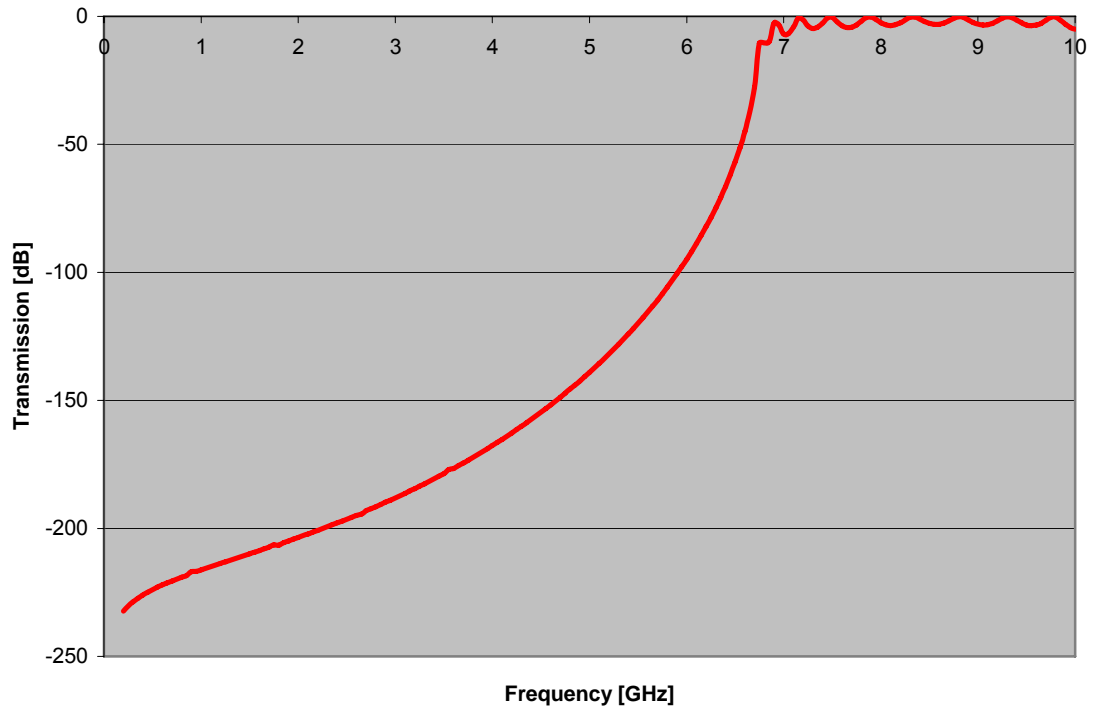
where  $17.5 \cdot 10^{-6}$  is the equivalent radius in meters of the wires; this value is calculated by taking the thickness of the layer of copper over a real substrate  $\approx 35\mu m$  and dividing it by two. The separation of the wires "a" can be called x-period according to Figure 2.13 and is the same as "l" or stacking sequence in sections 2.2 and 2.3.

In several papers [18] [20] [27], a good attenuation is achieved when the y-period is the same as the period of the SRRs. This design contains two SRR sizes hence two periods could apply, but since one size is one third of the other one, three small periods will exactly coincide with one big period. Therefore, by choosing the small period, which is 12.5mm (Figure 2.10), both small and big periods will be accomplished at the same time.

Figure 2.14a shows the simulation geometry of the preliminary thin-wire structure and Figure 2.14b computed results. Even though just one layer of wires produces the plasmon phenomenon, twelve layers of wires have been placed to clarify the exact value of the plasma frequency. The reader should notice that one layer of wires is simulated using just one wire and the master/slave BCs explained before. The geometry contains a substrate over which the wires are positioned; the substrate's thickness is 1.61mm and its relative permittivity is 2.17. The wire's thickness is 35 $\mu$ m that is thickness of the layer of copper over a real substrate; and its width is 0.5mm which is the narrowest strip the etching machine can manufacture. The wire is simulated as PEC.



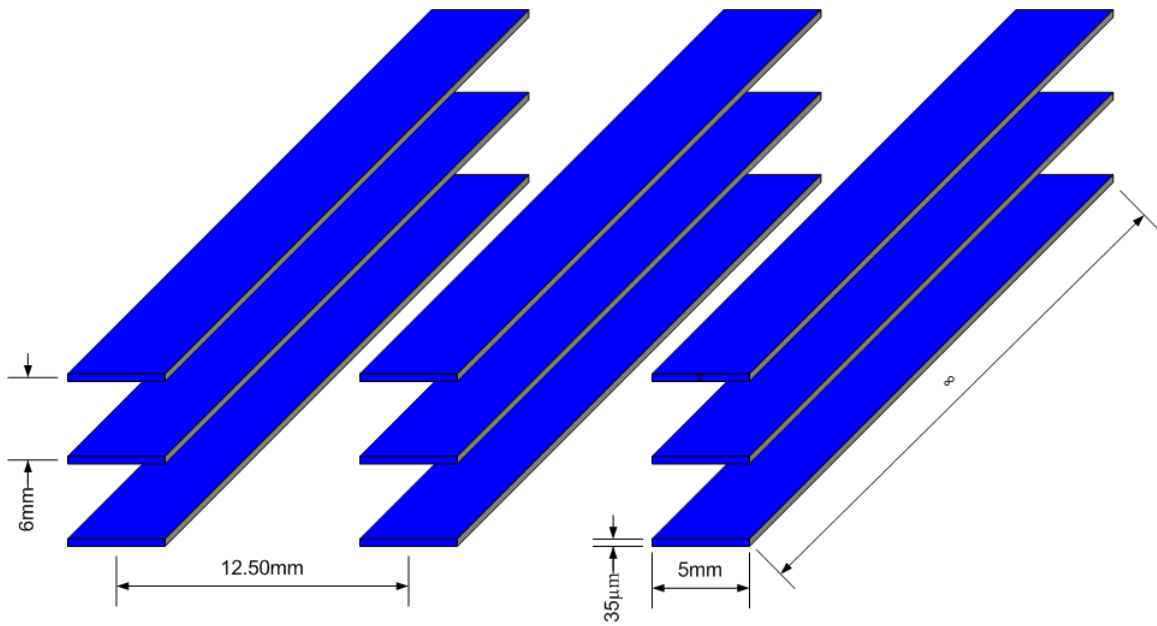
(a)



(b)

Figure 2.14.- (a) Snapshot of first thin-wire structure prototype. (b)  $S_{21}$ -parameter of the prototype.

From Figure 2.14b, the plasma frequency of the thin-wire structure is around 6.8GHz. This is slightly lower than the objective frequency (7.2GHz). Equation (1.7) suggests that the lower the  $x$ - period, the higher the plasma frequency, then, after a number of simulations, the plasma frequency is designed at 7.18GHz by dimensioning the wires as depicted in Figure 2.15.



(a)

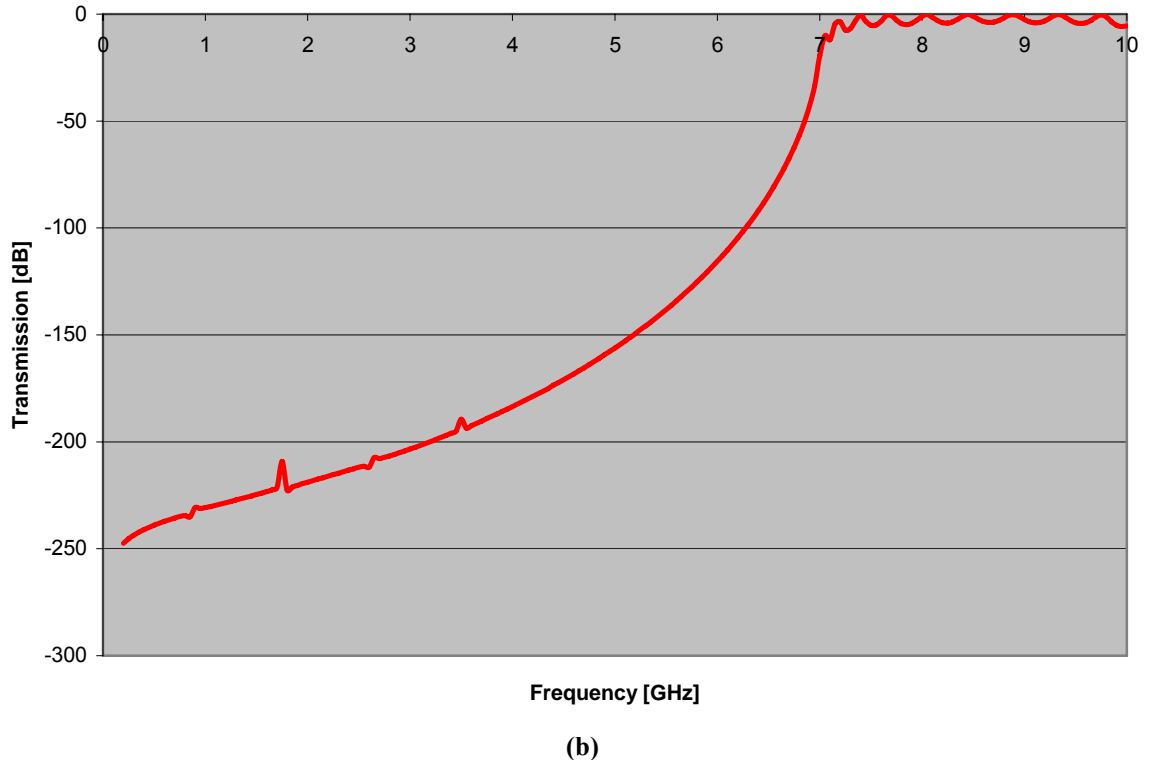


Figure 2.15.- (a) Dimensions of the thin-wire structure final design. (b) Its  $S_{21}$ -parameter.

## 2.5 Left-handed metamaterial simulation

As a last step in the design & simulation process, both designed structures, the Sierpiński-carpet-arranged SRRs and the thin-wire lattice, are put together to give rise to a left-handed Metamaterial. One can notice that while Sierpiński-carpet-arranged SRRs do not allow transmission at neither 5.03GHz nor 6.18GHz and the thin-wire structure does not allow transmission at frequencies lower than 7.18GHz; when they are put together

transmission appears at the frequencies where both do not allow transmission at the same time, namely 5.03GHz and 6.18GHz.

Less sharp pass bands are expected at the final simulation and in the experiment, compared to the sharpness of resonances obtained just from SRRs. When multiple unit cells are stacked along the direction of propagation, they interact among themselves and mutual coupling appears. This phenomenon along with other ones explained in [25] broaden the bandwidth and keep broadening it until around eight unit cells have been stacked. Beyond that point no additional bandwidth is gained and the S-parameters of the simulation converge.

Available computational resources allow the calculation of the S-parameters of just one unit cell of the entire LHM, nevertheless examples of convergence in eight unit cells for the rest of structures can be found in Appendix A.

The simulated LHM unit cell is a combination of a Sierpiński-carpet-arranged SRR unit cell on the top face of the substrate and three wires aligned with the SRRs on the bottom face (Figure 2.16a). The entire simulation environment is kept the same. Transmission ( $S_{21}$ ) of -0.48dB is achieved at 4.84GHz and -1.66dB at 6.10GHz; while the MTM and the surrounding vacuum are matched at 4.83GHz where the reflection coefficient ( $S_{11}$ ) has a dip of -17.70dB and at 6.10GHz where  $S_{11}$  is -8.65dB (Figure 2.16b).

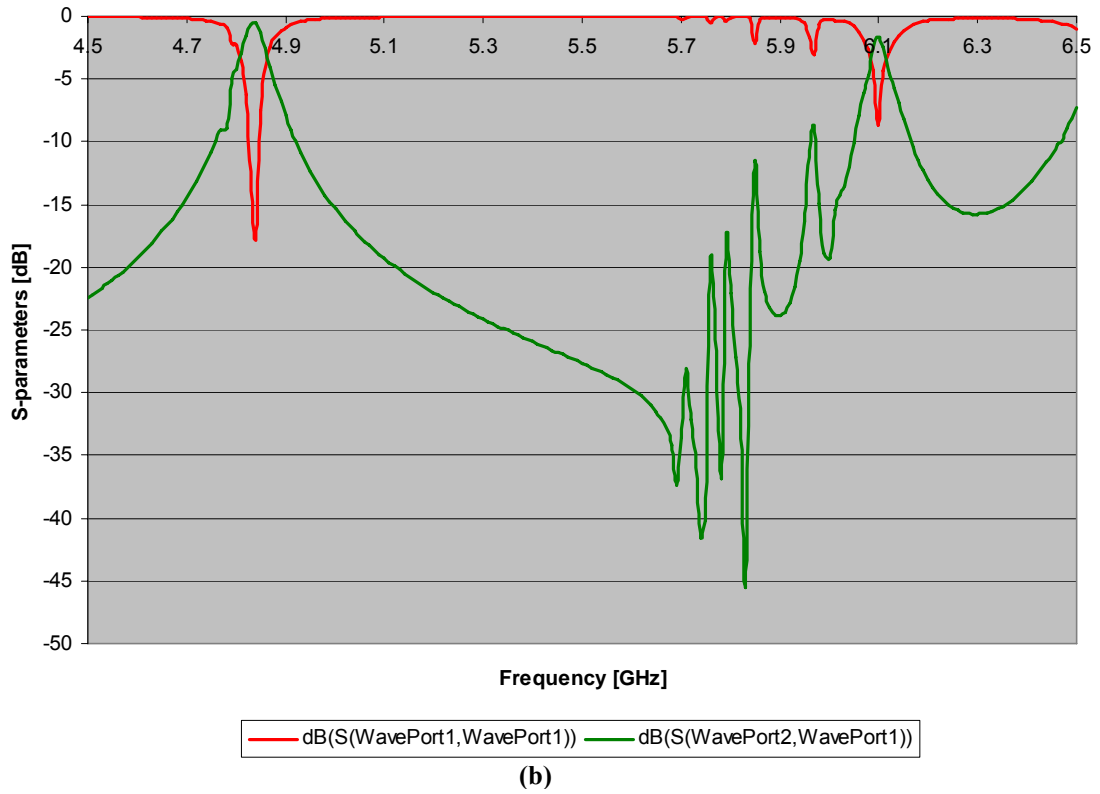
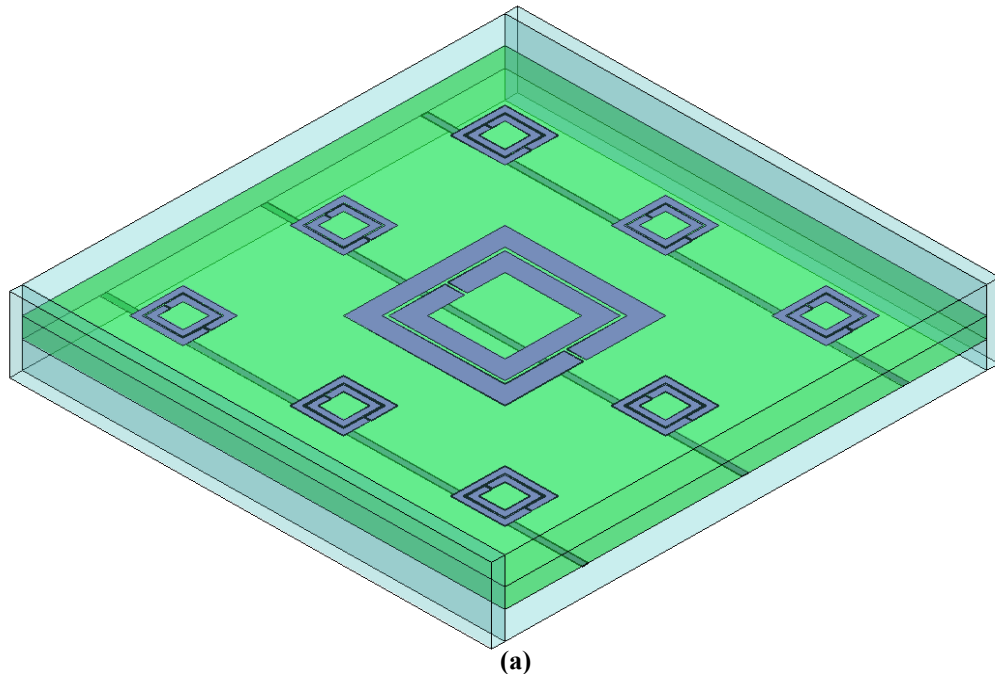


Figure 2.16.- (a) Designed left-handed metamaterial unit cell. (b)  $S_{11}$  and  $S_{21}$ -parameters of the designed LHM unit cell.

## **CHAPTER 3**

### **EXPERIMENTAL RESULTS**

For a better understanding of the previous chapters and in order to compare theory and simulations with practical results, two prototypes of the models simulated in Chapter 2 are manufactured and tested. The first prototype includes the large SRRs and the thin-wire structure and the second one includes the Sierpiński-carpet-arranged SRRs and the thin-wire structure.

Unlike simulations from Chapter 2, where the master/slave BCs simulated infinitely high and wide structures, in the practice, structures have finite dimensions. This is one of the reasons for discrepancies between simulations and experimental results.

The LHM is built by interleaving printed circuit board (PCB) slabs that host the models, and foam slabs that simulate air. Several steps are necessary to fabricate and test a LHM. First, PCBs are created by cutting slabs of substrate and mechanically etching them. Then, slabs of foam are cut and placed between the PCBs, and the whole structure is aligned, clamped and set up for measurements. Next, the reflection and transmission measurement setup is placed inside an anechoic chamber. The following sections will detail these steps by showing the procedure developed to measure the S-parameters.

### 3.1 PCB Fabrication

The PCB fabrication is accomplished by using a milling machine. The available machine is the LPKF ProtoMat® S62 shown in Figure 3.1. ProtoMat® S62 is a compact high-speed plotter used for single-sided, double-sided, multilayer mixed-signal, RF and microwave PCBs. It delivers a system resolution as fine as 0.25µm, its milling head travels at speed up to 150mm per second and it possesses a high-performance 62000RPM spindle motor.



Figure 3.1.- LPKF ProtoMat® S62.

Using the ProtoMat® S62 implies the use of the associated controlling software LPKF BoardMaster PCB 5.0 and this, in turn, the routing software LPKF CircuitCAM 5.0. LPKF CircuitCAM PCB provides a sophisticated CAM station; it can control all production data, modify the design, step and repeat the complete layout, perform different design rule checks, generate ground planes, input text using TrueType fonts, and generate routing data. LPKF BoardMaster handles milling and drilling data created by LPKF CircuitCAM and controls the PCB milling machine. For more detailed information about the use of the software, see [28]. Files generated by CircuitCAM (.cam & .lmd) and BoardMaster (.job) for both prototypes can be found in Appendix B.

Each CAD file evolution is as follows: HFSS simulation geometries from Chapter 2 (whose files can be found in Appendix A) need to be exported to the DXF format [29], then minor adjustments are performed using Autodesk® AutoCAD and the final .dxf file is opened using CircuitCAM which exports a .lmd file to BoardMaster for, finally, etching the PCB.

The substrate employed for the PCBs is Taconic® TLY-5A which has a dielectric constant of  $2.17 \pm 0.02$ , dissipation factor of 0.0009 @ 10GHz, copper thickness of 35 $\mu$ m, and dielectric thickness of 1.61mm. Further information of the dielectric can be found in [30]. Six pieces of substrate and five pieces of foam are cut for each prototype; each slab is 300mm x 112.5mm (roughly one fourth of A3 size) and contains twenty four unit cells,

which means that each prototype is made of one hundred forty four unit cells: three unit cells height, six unit cells width and eight unit cells thickness (Figure 3.2).

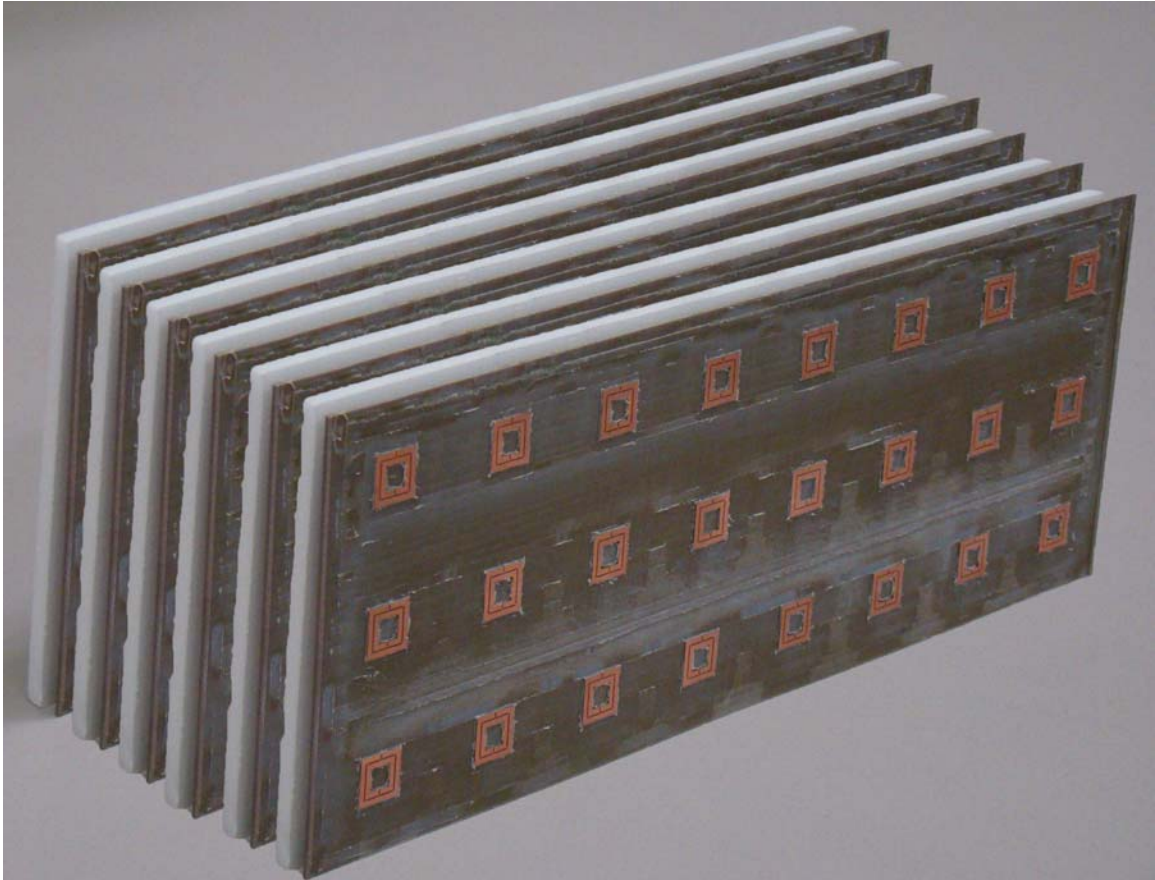


**Figure 3.2.- PCB and foam slabs.**

CircuitCAM is set to work with five milling tools whose diameters are: 0.10mm, 0.25mm, 0.40mm, 0.80mm and 3.00mm. They were chosen to produce optimum etching routes in terms of etching time and tool usage. Figure 3.3 shows the ProtoMat® S62 during the etching process.

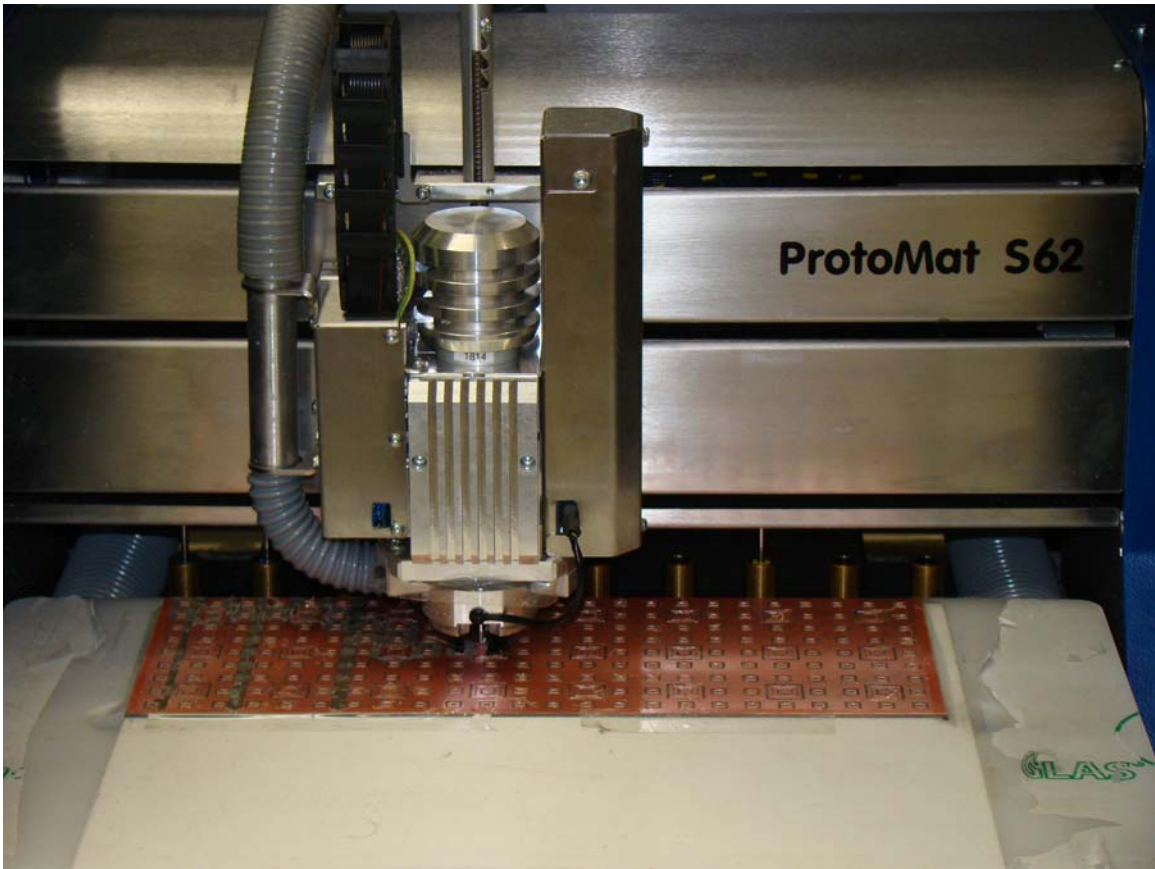
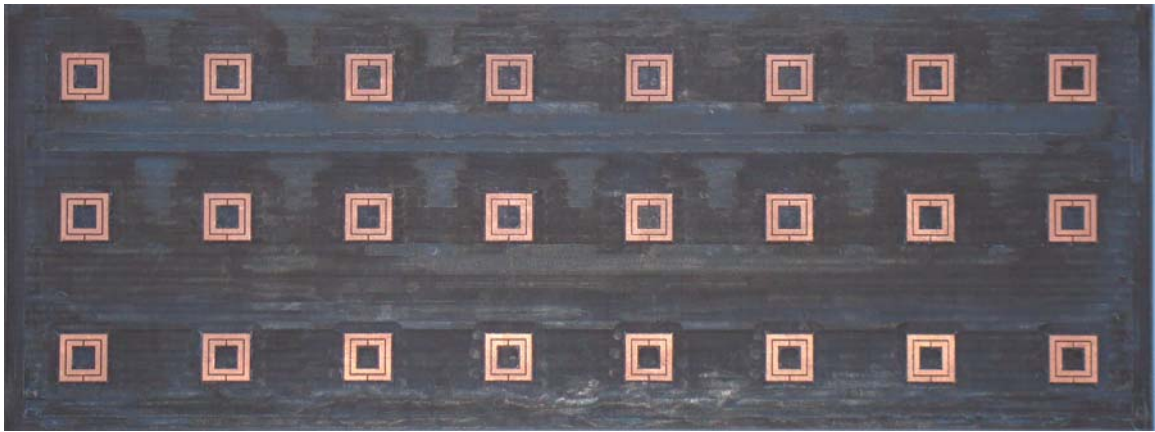


**Figure 3.3.- Etching process.**

The procedure is repeated on the top face for the other five PCB pieces to etch the SRR lattice; then they are flipped to the other side and the thin-wire structure is also etched. To finish, using the other simulated geometry, another six PCB pieces for the second prototype are etched. Figure 3.4 shows both faces of the obtained PCB using only the large SRRs; Figure 3.5 shows the PCB using the Sierpiński-carpet-arranged SRRs.

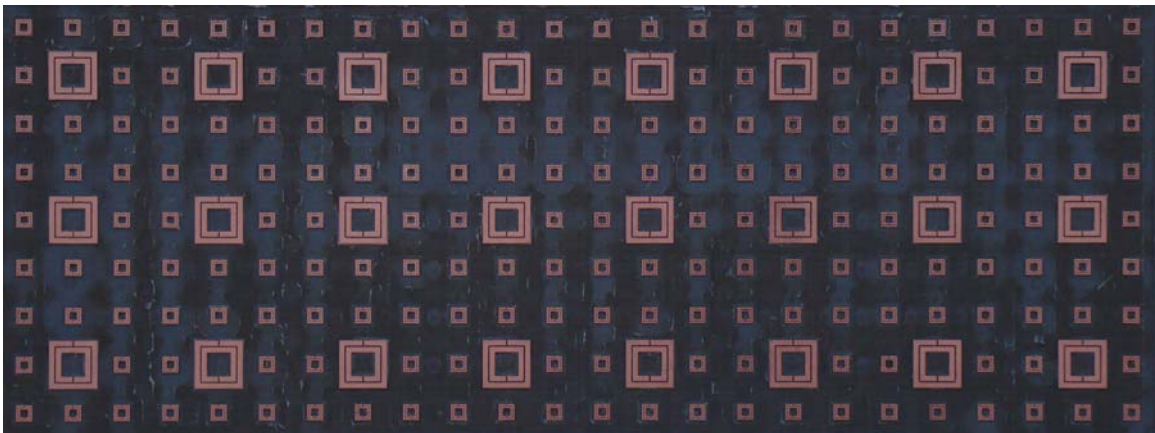


(a)



(b)

**Figure 3.4.- Both sides of an etched PCB of the first prototype. (a) Large SRRs lattice. (b) Thin-wire structure.**



(a)



(b)

**Figure 3.5.- Both sides of an etched PCB of the second prototype. (a) Sierpiński-carpet-arranged SRRs lattice. (b) Thin-wire structure.**

### **3.2 S-parameters measurement setup**

Two setups are required to take measurements of the fabricated LHM. The first one was briefly explained in the previous section and it is related to the stacking of the PCBs and a clamping mechanism. The second setup corresponds to the equipment and facilities for the measurement such as an anechoic chamber, transmitter and receiver antennas, a network analyzer, etc.

A important problem to face during the final stage of the LHM's fabrication is stacking the PCBs in such a way that they are in parallel and the period between PCBs is 6mm while the relative permittivity of the medium between the boards is kept at 1 (same as air); all at the same time. Many possibilities were tested: Holding PCBs from the corners, holding them from their edges, partially inserting PCBs into foam slabs, making grooves

on foam slabs and placing the boards inside them, etc. These solutions either do not keep the boards straight and parallel or do not allow placing them at exact intervals of 6mm. The best solution in terms of ease, effectiveness and cost is selecting foam slabs of several thicknesses and stacking them until the right thickness is achieved, then, cutting the slabs using the PCBs' dimensions, and finally, interleaving foam and PCBs while keeping them aligned. The alignment is a crucial issue when stacking PCBs, especially when stacking the ones of the second prototype. SRRs and wires of different layers have to be exactly one on top of each other in order to obtain a homogeneous MTM to propitiate strong and clear resonances. The alignment task is performed with the greatest possible care because a misalignment of 0.1mm between to adjacent small rings compared to the ring's width (0.5mm) is an effective misalignment of 20%. The last step is to carefully clamp the entire structure; this can also be done in several ways, the simplest is to fasten it with several loops of a thin non-conducting highly-adhesive tape. Figure 3.6 and Figure 3.7 show the prototypes already tied up and ready to measure.

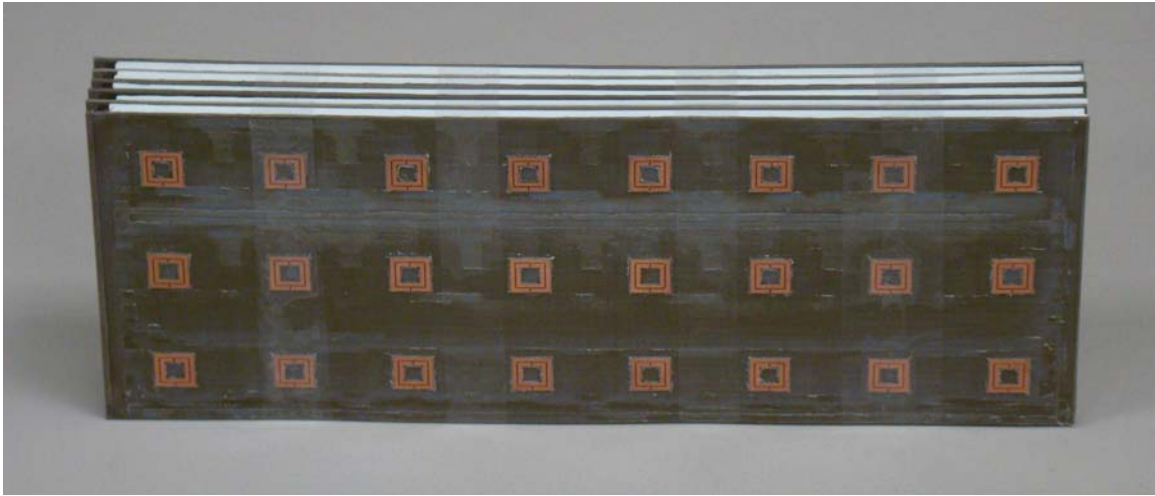


**Figure 3.6.- First MTM prototype ready to be measured.**

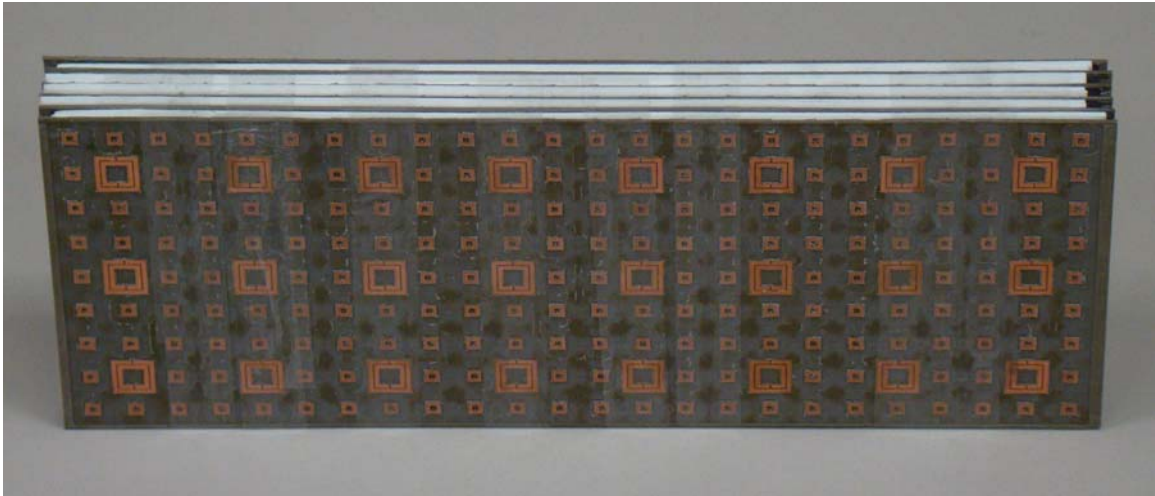


**Figure 3.7.- Second MTM prototype ready to be measured.**

In order to take the best possible measurements of the LHM's response, special care must be taken to avoid interferences and undesired propagation modes. Measurements have to be carried out inside an anechoic chamber to avoid interference from external sources as well as from multi-path propagation while taking data. The uniform plane wave required

to illuminate the LHM is generated using an SMA-to-waveguide transition and a horn antenna of the G WFB whose lowest recommended frequency is 3.95GHz (less than the first resonance, 4.84GHz); the antenna is placed far enough so only the far field impinges the MTM. Having the higher resonance at 6.10GHz, the far field distance is  $\frac{2D^2}{\lambda} = \frac{2D^2 f}{c} = \frac{2 \cdot 0.2^2 \cdot 6.10 \cdot 10^9}{3 \cdot 10^8} = 1.63m$  [31]. The LHM is located roughly at that distance ( $\approx 1.70m$ ) from the transmitter and aligned to the center of the horn antennas by using a foam table specially made for this purpose. The receiver is just a detector implemented with a waveguide-to-SMA transition that is positioned right behind the LHM block. Non-conductive pedestals for both, transmitter and receiver are used to avoid interference. Figure 3.8 displays the entire setup used.

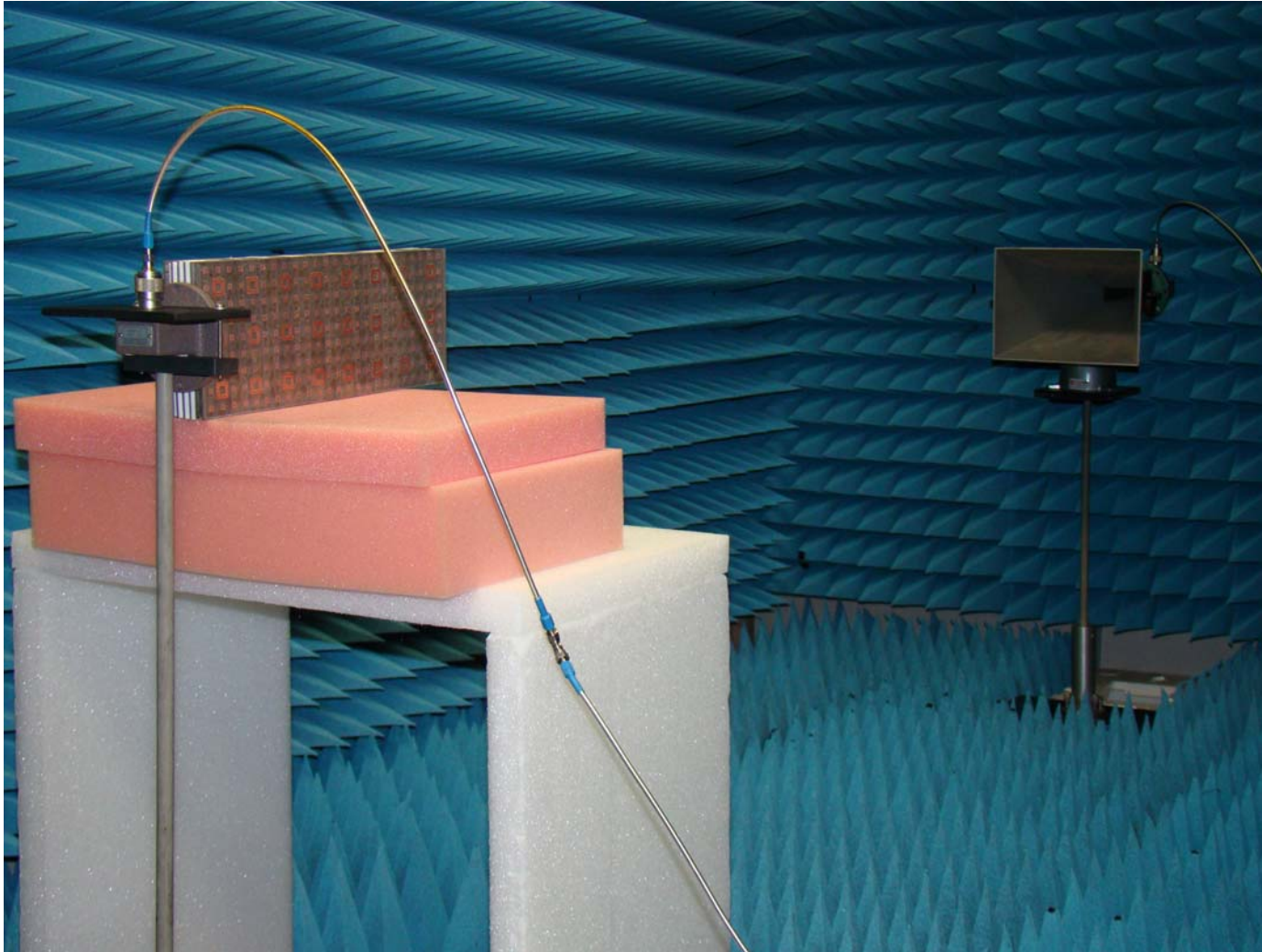


**Figure 3.8.- Setup for measurement.**

### 3.3 Measurements

The final stage of the project consists in collecting data from the prototypes by measuring their S-parameters through the setup explained earlier. The Agilent 8510C VNA is used to measure the transmission ( $S_{21}$ ) parameter. The Agilent 8510C VNA includes the Agilent 8517B Synthesized Sweeper which is able to sweep frequencies from 45MHz to 50GHz; consequently the VNA is also capable of working within the same range.

For the first prototype (large SRRs and wires), the transmission coefficient obtained from the VNA is shown in Figure 3.9. The peak transmission is -8.51dB and it is found at 4.8375GHz, virtually the same as the resonance frequency from simulations, 4.84GHz. However, transmission in the ideal simulation (-0.48dB) is higher than the measured one.

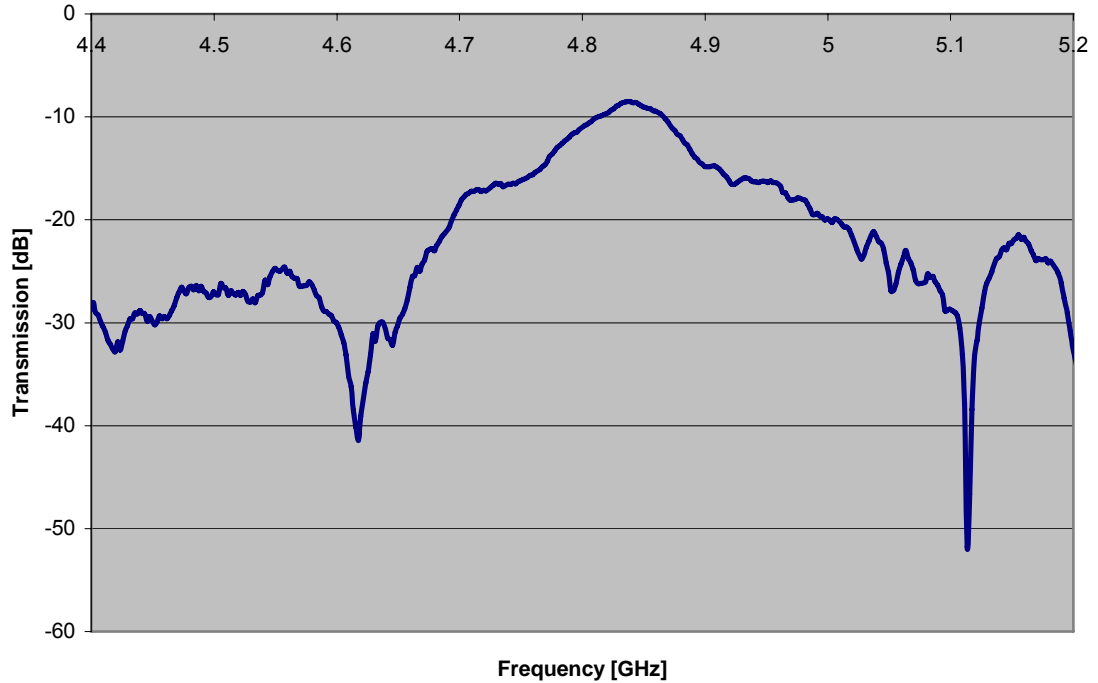


**Figure 3.9.- Measured  $S_{21}$  parameter of the first prototype.**

The second prototype is measured under the same conditions; and the results are shown in Figure 3.10. As expected from simulations, two transmission peaks are found: a peak of -10.29dB is located at 4.785GHz and another peak of -12.03dB at 6.145GHz. The measured and simulated resonances agree very well but the values of the transmission are stronger in simulations (-0.48dB @ 4.84GHz and -1.66dB @ 6.10GHz).

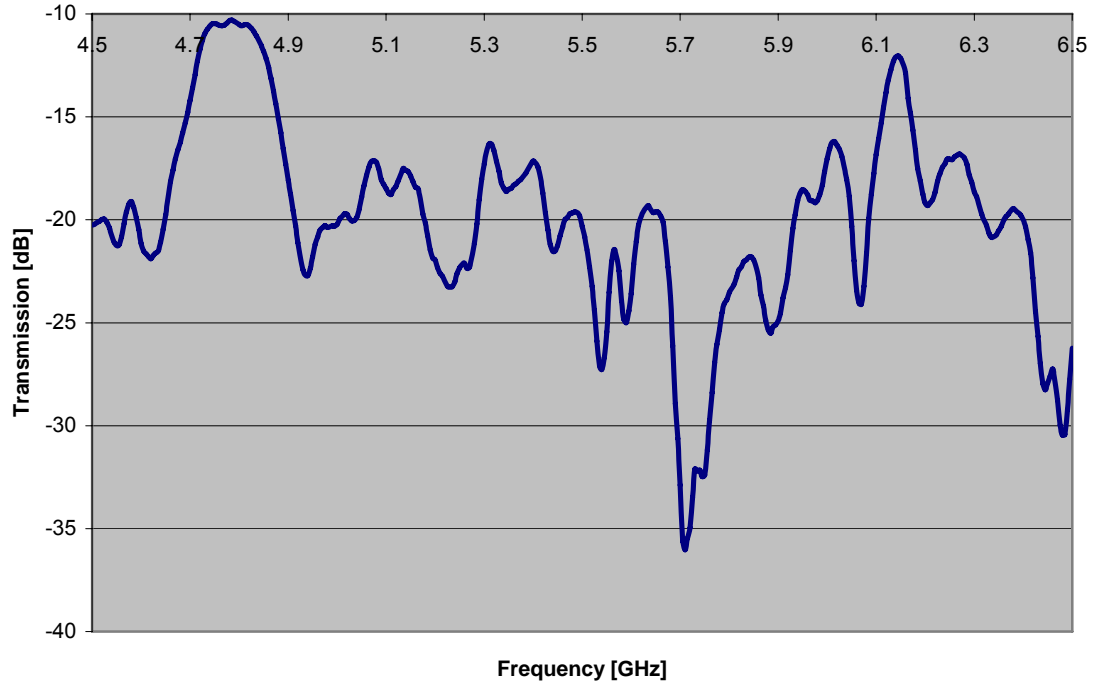


**Figure 3.10.- Measured  $S_{21}$ -parameter of the second prototype.**

### **3.4 Comparison and conclusions**

This work gives some insight into the behavior of a real finite LHM and a number of conclusions can be made when it is compared to an ideally simulated LHM. Figure 3.11 compares the results from Figures 2.16b and 3.10 and helps to compare the ideal and actual responses of LHM.

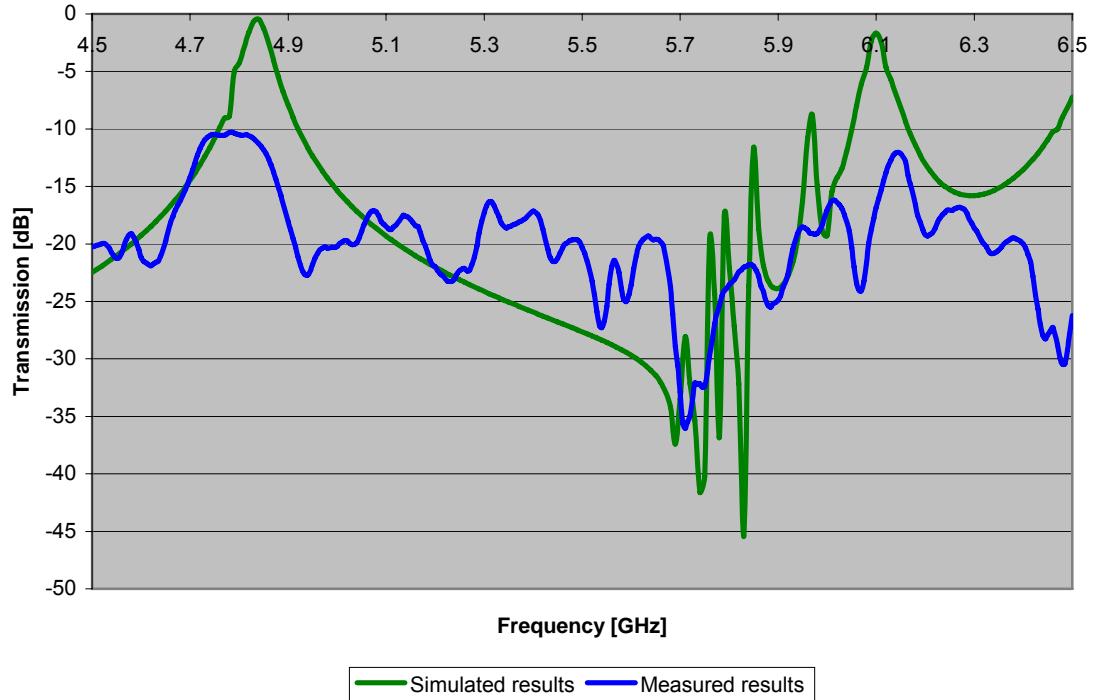


**Figure 3.11.- Simulated and measured  $S_{21}$ -parameter**

The most important characteristic of the curves in Figure 3.11 are their peaks of transmission. The two peaks are the most important goal of this thesis because they provide the bandwidths where a signal can be transmitted through the MTM undergoing left-handed propagation inside it. Two peaks appear in both the simulated and the measured results curves. Hence the principle of left-handed propagation is experimentally demonstrated.

Perhaps the most evident difference between the curves in Figure 3.11 is the level of transmission. At the first peak, simulation exhibits transmission of -0.48dB, while measurements exhibit only -10.29dB; at the second one, simulations exhibits -1.66dB and

measurements -12.03dB. In simulations, the receiver is a perfectly flat rectangular area known as port (see Chapter 2); the port acts as an ideal receiver, which means that every single point over its surface has an isotropic radiation pattern in the outward direction. Thus, this port is a hypothetical lossless antenna having equal radiation in every outward direction. The waveguide-to-SMA transition (Figure 3.12) used as receiver for measurements is a real device with losses. It has a radiation pattern with a main lobe oriented perpendicularly to the center point of its aperture, side lobes in other directions and essentially no reception near to the lateral edges. Moreover, this device does not measure TEM waves directly, but first transforms it into a TE wave causing more losses. This factor by itself significantly attenuates the signal, but other reasons can also cause a discrepancy between measurements and simulations. Misalignments between layers and imperfections in SRRs (will be explained shortly), foam which separates PCBs that does not perform exactly as air, bumps, grooves and other irregularities on the PCB's surfaces, debris and chips that remained stuck to the PCBs after the etching process, and undesired adhesive tape are several reasons that keep the structure from having transmission as good as in simulations.



**Figure 3.12.- Waveguide-to-SMA transition.**

The resonance frequencies that were determined by the simulations and the experiments are practically the same. In simulations the first peak appears at 4.84GHz, whereas in the experiment it appears at 4.785GHz (98.9% of accuracy). In simulations the second peak emerges at 6.10GHz and in measurements at 6.145GHz (99.2% of accuracy).

The transmission bandwidth is another important parameter to discuss. At the first peak, simulations show a -3dB bandwidth of 60MHz and the experiments show a bandwidth of 170MHz. The reason why the experimental results are better than the simulated ones is that it was used only a one-unit-cell-thick LHM to simulate the periodic structure

whereas the entire eight-unit-cell-thick fabricated structure was used in the measurements. It was anticipated that a simulated model that takes into consideration at least eight unit cells will yield results that are closer to the experimental ones in terms of bandwidth because, coupling among SRRs along the direction of propagation improves the bandwidth. At the second peak, a similar reason justifies -3dB bandwidths of 40MHz for simulations and 60MHz for the measured model. If both bandwidths are brought together by means of the reconfigurable technique previously proposed this LHM can outperform any other classic design of LHM, yielding a bandwidth of at least 230MHz.

On the high frequency side of the measured second peak, a multi resonance phenomenon is observed. Two mysterious peaks appear at 6.275GHz and 6.385GHz; they are not only undesired but because they are misplaced far from the main resonance (6.145GHz), they do not contribute to it and weaken the transmission characteristics of the structure. This major problem has two reasons: misalignments between layers and imperfections in SRRs. Misalignments between layers are almost unavoidable; however alignment is crucial when stacking PCBs. SRRs and wires of different layers have to be exactly one on top of each other in order to obtain a homogeneous MTM to generate strong and clear resonances. For example, a single misalignment of 0.1mm between two adjacent small SRRs compared to the ring's width (0.5mm) yields an effective misalignment of 20%. Even though the greatest care was taken to line up all the rings, it is not possible to get such a precision without specialized tools. Imperfections during the SRR manufacture are also a reason for the multiple resonances. Due to tolerance problems during fabrication,

some ring gaps and ring splits can be etched wider than they should be. This causes the resonance frequency to slightly shift towards higher frequencies.

Finally, some peaks, which do not exist in simulations, are noticeable in the measured data between 5GHz and 5.7GHz. Although they are 5dB below the main transmission peaks, in order to eliminate them a bigger model is required. Since the real model is not infinite in extend as the simulated model, diffraction takes place on the edges of the structure. Diffraction, along with power leakages around the prototype are the reasons for this behavior.

The overall response of the fabricated LHM is very consistent with what was predicted from simulations and theory, and fulfills the expectations. Peaks of transmission appeared where they were designed to appear and the goal of enhancing the volumetric LHM bandwidth by introducing the Sierpiński-carpet fractal pattern and the reconfigurability capability was fully accomplished and demonstrated.

## CONCLUSIONS AND FUTURE WORK

This thesis presented the computational analysis and design as well as experimental results for Left-handed Metamaterials. The simulation process and design criteria required to increase the bandwidth of LHMs were included and explained in details. The merits and possibilities of designing reconfigurable left-handed metamaterials have also been discussed in this thesis.

By introducing the Sierpiński carpet fractal pattern and the reconfigurability capability, it was demonstrated that the bandwidth for a LHM can be increased. It was shown that it is possible to increase the effective LHM transmission bandwidth through reconfigurability by setting two SRR resonances close enough that they partially overlap and, at the same time, dimensions of SRRs can be efficiently used to perform fine tunings of the resonance frequency. The two transmission bands designed and simulated have shown good agreement with the measured data. The same principle was also verified experimentally.

For future research work, it is important to use real models of switches which will have to include their biasing effects on the transmission and reflection characteristics of the entire MTM structures. Future simulations can benefit by more computational power in order to obtain faster and more precise results, and analyze more complicated fractal patterns. Subsequent PCBs should be chemically etched over a substrate firmer and more

rigid than Taconic TLY-5A and they should be appropriately clamped since high-quality results are greatly influenced by the precision and reliance of the procedures performed.

## APPENDIX

### Appendix A: HFSS Simulation files (in attached CD)

- Environment.hfss.- PEC and PMC boundary condition tests, master/slave boundary condition tests, final design of a plane wave generator ports, final design of the complete environment.
- Thin\_wire.hfss.- Single wire tests varying height and width, multiple wire tests varying periods in x and y directions, effect of the number of wires (convergence in about eight wires), final design of thin-wire structure.
- Separation.hfss.- Effect of the separation among SRRs in directions x, y and z.
- Circular\_SRR.hfss.- Tests using circular SRRs.
- SRR.hfss.-Tests varying the distances and lengths of large and small SRRs, effect of the number of SRRs (convergence in about eight SRRs), final SRR designs.
- Reconfigurable\_SRR.hfss.- Tests related to SRR's sensitivity to the splits' location, final design of reconfigurable SRRs.
- Fractal.hfss.- Tests using Sierpiński-carpet-arranged SRRs varying simulation parameters to optimize computational resources.
- LHM.hfss.- Final design of the two LHM prototypes.

## **Appendix B: Autocad & PCB files (in attached CD)**

- Prototype1\_top.dxf & Prototype1\_bottom.dxf.- First prototype's final geometry in Autocad.
- Prototype2\_top.dxf & Prototype2\_bottom.dxf.- Second prototype's final geometry in Autocad.
- Prototype1.cam.- First prototype's final routing generated by CircuitCAM.
- Prototype2.cam.- Second prototype's final routing generated by CircuitCAM.
- Prototype1.lmd.- First prototype's etching instructions generated by CircuitCAM.
- Prototype2.lmd.- Second prototype's etching instructions generated by CircuitCAM.
- Prototype1.job.- First prototype's settings for BoardMaster.
- Prototype2.job.- Second prototype's settings for BoardMaster.

## REFERENCES

- [1] I. V. Lindell et al., "Karl F Lindman: The last Hertzian, and a Harbinger of electromagnetic chirality", *IEEE Antennas Propag. Mag.*, vol 34, no. 3, pp. 24-30, 1992.
- [2] W. E. Kock, "Metalic delay lenses", *Bell Sys. Tech. J.*, vol. 27, pp.58-82, 1948.
- [3] V. G. Veselago, "The electrodynamics of substances with simultaneously negative values of  $\epsilon$  and  $\mu$ ", *Sov. Phys. Uspekhi*, vol. 10, no. 4, pp.509-514, 1968.
- [4] D. R. Smith and N. Kroll, "Negative refractive index in left-handed materials", *Phys. Rev. Lett.*, vol. 85, pp. 2933-2936, 2000.
- [5] N. Engheta, "An idea for thin subwavelength cavity resonators using metamaterials with negative permittivity and permeability", *IEEE Antennas Wireless Propag. Lett.*, vol. 1, pp. 10-13, 2002.
- [6] R. A. Shelby et al., "Experimental verification of a negative index of refraction", *Science*, vol. 292, no. 5514, pp. 77-79, 2001.

- [7] A. Alu and N. Engheta, "Guided in a waveguide filled with a pair of single-negative (SNG), double-negative (DNG) and/or double-positive layers", *IEEE Trans. Microwave Theory Tech.*, vol. MTT-52, no. 1, pp. 199-210, 2004.
- [8] J. B. Pendry, "Negative refraction makes a perfect lens", *Phys. Rev. Lett.*, vol. 85, no. 18, pp. 3966–3969, 2000.
- [9] A. A. Grbic and G. V. Eleftheriades, "Experimental verification of backward-wave radiation from a negative refractive index metamaterial", *J. Appl. Phys.*, vol. 92, pp. 5930–5935, 2002.
- [10] J. Lu et al., "Cerenkov radiation in materials with negative permittivity and permeability", *Opt. Express*, vol. 11, pp. 723–734, 2003.
- [11] Z. M. Zhang and C. J. Fu, "Unusual photon tunneling in the presence of a layer with negative refractive index", *Appl. Phys. Lett.*, vol. 80, pp. 1097–1099, 2002.
- [12] R. W. Ziolkowski and A. Kipple, "Application of double negative metamaterials to increase the power radiated by electrically small antennas", *IEEE Trans. Antennas Propag.*, vol. 51, no. 10, pp. 2626–2640, 2003.
- [13] J. B. Pendry, "Extremely low frequency plasmons in metallic mesostructures", *Phys. Rev. Lett.*, vol. 76, pp. 4773-4776, 1996.

- [14] J. B. Pendry et al., "Magnetism from conductors and enhanced nonlinear phenomena", *IEEE Trans. Microwave Theory Tech.*, vol. 47, no. 11, pp. 2075-2084, 1999.
- [15] D. R. Smith et al., "Composite medium with simultaneously negative permeability and permittivity", *Phys. Rev. Lett.*, vol. 84, pp. 4184-4187, 2000.
- [16] N. Engheta and R. W. Ziolkowski, "Metamaterials, physics and engineering explorations", *IEEE Press*, 2006.
- [17] R. W. Ziolkowski and F. Auzanneau, "Passive artificial molecule realizations of dielectric materials", *J. Appl. Phys.*, vol. 82, no. 7, pp. 3195–3198, 1997.
- [18] K. Aydin and E. Ozbay, "Experimental investigation of reflection characteristics of left-handed metamaterials in free space", *IET Microw. Antennas Propag.* vol. 1, pp. 89-93, 2007.
- [19] R. W. Ziolkowski, "Design, fabrication and testing of double negative metamaterials", *IEEE Trans. Antennas Propag.*, vol. 51, no. 7, pp. 1516–1529, 2003.
- [20] D. R. Smith et al., "Design and measurement of anisotropic metamaterials that exhibit negative refraction", *IEICE Trans. Electron.*, vol. E87-C, no. 3, 2004.

- [21] [http://en.wikipedia.org/wiki/Sierpinski\\_carpet](http://en.wikipedia.org/wiki/Sierpinski_carpet)
- [22] K. Aydin et al., "Investigation of magnetic resonances for different split-ring resonator parameters and designs", *New Journal of Physics*, vol. 7, no.168, 2005.
- [23] R. E. Mihailovich, "MEM relay for reconfigurable RF circuits", *IEEE Microwave and Wireless Components Letters*, vol. 11, no. 2, 2001.
- [24] J. DeNatale, "Reconfigurable RF circuits based on integrated MEMS switches", *IEEE International Solid-State Circuits Conference*, session 17, no. 1, 2004.
- [25] P. Gay-Balmaz and O. Martin, "Electromagnetic resonances in individual and coupled split-ring resonators", *Journal of Applied Physics*, vol. 92, no. 5, 2002.
- [26] [http://en.wikipedia.org/wiki/Paper\\_size](http://en.wikipedia.org/wiki/Paper_size)
- [27] C. T. Chevalier and J. D. Wilson, "Frequency bandwidth optimization of left-handed material", *NASA/TM*, no. 213403, 2004.
- [28] <http://www.lpkfusa.com/Software/index.htm>
- [29] <http://en.wikipedia.org/wiki/Dxf>

[30] <http://www.taconic-add.com/en--products--tly--1.php>

[31] C. A. Balanis, "Antenna Theory, analysis and design. Third Edition", Wiley-Interscience, 2005.